

Recognition of methamphetamine and other amines by trace amine receptor TAAR1

<https://doi.org/10.1038/s41586-023-06775-1>

Received: 5 May 2023

Accepted: 20 October 2023

Published online: 7 November 2023

 Check for updates

Heng Liu^{1,12}, You Zheng^{2,12}, Yue Wang^{1,3,12}, Yumeng Wang^{3,4,12}, Xinheng He^{1,3}, Peiyu Xu^{1,3}, Sijie Huang^{1,3}, Qingning Yuan^{1,5}, Xinyue Zhang^{1,6}, Ling Wang², Kexin Jiang², Hong Chen^{7,8}, Zhen Li^{1,6}, Wenbin Liu^{7,8}✉, Sheng Wang^{4,9}✉, H. Eric Xu^{1,3,10}✉ & Fei Xu^{2,11}✉

Trace amine-associated receptor 1 (TAAR1), the founding member of a nine-member family of trace amine receptors, is responsible for recognizing a range of biogenic amines in the brain, including the endogenous β -phenylethylamine (β -PEA)¹ as well as methamphetamine², an abused substance that has posed a severe threat to human health and society³. Given its unique physiological role in the brain, TAAR1 is also an emerging target for a range of neurological disorders including schizophrenia, depression and drug addiction^{2,4,5}. Here we report structures of human TAAR1–G-protein complexes bound to methamphetamine and β -PEA as well as complexes bound to RO5256390, a TAAR1-selective agonist, and SEP-363856, a clinical-stage dual agonist for TAAR1 and serotonin receptor 5-HT_{1A}R (refs. 6,7). Together with systematic mutagenesis and functional studies, the structures reveal the molecular basis of methamphetamine recognition and underlying mechanisms of ligand selectivity and polypharmacology between TAAR1 and other monoamine receptors. We identify a lid-like extracellular loop 2 helix/loop structure and a hydrogen-bonding network in the ligand-binding pockets, which may contribute to the ligand recognition in TAAR1. These findings shed light on the ligand recognition mode and activation mechanism for TAAR1 and should guide the development of next-generation therapeutics for drug addiction and various neurological disorders.

Methamphetamine (METH) is among the top ten addictive substances involved in overdose deaths and poses a severe threat to human health and the society³. This potent synthetic psychostimulant is known to cause substantial long-term damage to the body, including cognitive impairment, cardiovascular dysfunction, increased risk of infectious disease transmission and even psychosis^{8,9}. Despite its prevalence and impact on public health worldwide, there are currently no US Food and Drug Association-approved medications to treat METH addiction¹⁰. Therefore, discovering potential targets involved in the METH signalling pathway and developing effective pharmacotherapies to address psychostimulant addiction stand as pressing medical needs².

METH's impact on the brain's dopamine system results in behavioural and neurotoxic effects by boosting dopamine release in the synaptic cleft and hindering dopamine reuptake via the dopamine transporter (DAT) and vesicular monoamine transporter (VMAT)^{9,11}. Recent studies have shed light on an additional facet of METH's actions, revealing its role as a potent agonist of the trace amine-associated receptor 1 (TAAR1)¹². TAAR1 is a G-protein-coupled receptor (GPCR) primarily located intracellularly¹³. Trace amines, the endogenous agonists of

TAAR1, represent a series of brain amines structurally similar to classical biogenic amine, including tyramine, β -phenylethylamine (β -PEA), octopamine and tryptamine, which play crucial roles in modulating monoaminergic neuron physiology^{14–16}. Among these, β -PEA stands out as the brain's 'endogenous' amphetamine due to its ability to induce amphetamine-like effects, particularly at high doses¹⁴.

While METH's impact on dopamine release and reuptake is well-documented, the discovery of METH's binding to TAAR1 adds an additional layer of complexity to its neurobiological effects⁹. TAAR1 appears to play a modulatory role in the neurobiological effects of METH, potentially influencing the development of METH addiction^{11,12}. Previous studies indicated that the activation of TAAR1 mitigates psychostimulant-abuse-related behaviours, whereas the knockout of TAAR1 enhances such behaviours¹⁷, signifying the pivotal role of TAAR1 in the modulation of psychostimulant addiction^{2,18}. Activation of TAAR1 by agonists like METH initiates a signalling cascade that involves the accumulation of cyclic adenosine monophosphate (cAMP) through the activation of the G_s pathway^{12,19}. This signalling cascade has implications for the trafficking of dopamine and glutamate transporters

¹The State Key Laboratory of Drug Research, Shanghai Institute of Materia Medica, Chinese Academy of Sciences, Shanghai, China. ²Human Institute, School of Life Science and Technology, ShanghaiTech University, Shanghai, China. ³University of Chinese Academy of Sciences, Beijing, China. ⁴State Key Laboratory of Molecular Biology, Shanghai Institute of Biochemistry and Cell Biology, Center for Excellence in Molecule Cell Science, Chinese Academy of Sciences, Shanghai, China. ⁵The Shanghai Advanced Electron Microscope Center, Shanghai Institute of Materia Medica, Chinese Academy of Sciences, Shanghai, China. ⁶School of Chinese Materia Medica, Nanjing University of Chinese Medicine, Nanjing, China. ⁷Shanghai Key Laboratory of Crime Scene Evidence, Shanghai Research Institute of Criminal Science and Technology, Shanghai, China. ⁸Shanghai Yuansi Standard Science and Technology Co., Ltd, Shanghai, China. ⁹Key Laboratory of Systems Health Science of Zhejiang Province, School of Life Science, Hangzhou Institute for Advanced Study, University of Chinese Academy of Sciences, Hangzhou, China. ¹⁰School of Life Science and Technology, ShanghaiTech University, Shanghai, China. ¹¹Shanghai Clinical Research and Trial Center, Shanghai, China. ¹²These authors contributed equally: Heng Liu, You Zheng, Yue Wang, Yumeng Wang. [✉]e-mail: wbliu1981@163.com; wangsheng@sibcb.ac.cn; eric.xu@simm.ac.cn; xufei@shanghaitech.edu.cn

Article

within dopamine neurons^{12,13}. Considering TAAR1's pivotal role in modulating the effects of METH and other psychostimulants, it has emerged as a prospective target for addiction treatment. However, the precise mechanisms underpinning these effects necessitate further in-depth investigation^{2,4,12,18}.

TAAR1 is the founding member of the nine-member TAAR family of GPCRs, divided into three subfamilies: TAARs 1–4, TAAR5 and TAARs 6–9, among which six members (TAAR1, 2, 5, 6, 8 and 9) have been confirmed as functional in the human genome^{1,20}. TAAR1 has garnered the most extensive examination due to its capacity to respond to various biogenic amines and psychoactive compounds^{5,21}. Unlike other TAARs, which are primarily expressed in olfactory regions²², TAAR1 manifests widespread presence across the mammalian brain, particularly in monoaminergic nuclei and their associated projecting areas²¹. The expression of TAAR1 in areas where dopaminergic (ventral tegmental area (VTA), substantia nigra pars compacta (SNpc)), serotonergic (dorsal raphe and VTA), and glutamatergic (cortex, amygdala and subiculum) neurons¹ originate aligns with studies that underscore the pivotal role of TAAR1 in the modulation of reward circuits, limbic networks, cognitive processes and mood states^{4,23,24}. Beyond its presence in specific brain regions, TAAR1 also finds expression in peripheral tissues integral to the regulation of energy metabolism and immune functions^{4,25}.

TAAR1's unique physiological activity in the brain has spurred numerous in vitro and in vivo studies investigating the potential of TAAR1 agonists as treatments for various diseases, including schizophrenia, depression, bipolar disorder and drug addiction^{2,4,5,15,16,25,26}. Roche has developed several synthetic compounds targeting TAAR1, including five selective agonists: RO5256390, RO5166017, RO5263397, RO5073012 and RO5203648 (refs. 27,28). RO5256390, a potent and selective agonist of TAAR1, has demonstrated activity in various behavioural models of psychiatric disorders, such as schizophrenia and mood disorders^{25,29}. RO5256390 has been shown to inhibit cocaine-induced hyperlocomotion, suppress cocaine-seeking behaviour and reduce relapse triggered by either drug-related cues or the drug itself^{25,30}.

Another clinical-stage drug molecule, SEP-363856 (ulotaronet)^{6,7}, exhibits agonist activity at both TAAR1 and 5-hydroxytryptamine type 1A (5-HT_{1A}) receptors, potentially representing a new class of psychotropic agents for treating psychosis in schizophrenia⁷. In a phase 2 trial involving individuals with acute exacerbation of schizophrenia, SEP-363856 demonstrated efficacy compared with placebo. Additionally, SEP-363856 displayed very low rates of extrapyramidal, metabolic and other side effects typically associated with current antipsychotics⁶. Thus, TAAR1 agonism and its associated polypharmacology may offer a novel paradigm for neuropsychiatric and drug addiction therapeutics^{2,4,5}.

Considering the direct interaction between METH and TAAR1, as well as TAAR1's diverse physiological functions in the human body, understanding the molecular mechanisms involved in METH and TAAR1 agonist binding is crucial. The potential therapeutic value of TAAR1 agonists further emphasizes the importance of elucidating their underlying mechanisms of action. Here, we report four cryo-electron microscopy (cryo-EM) structures of human TAAR1–G_s protein complexes with METH, the endogenous ligand β-PEA, selective agonist RO5256390 and SEP-363856, respectively. In addition, we determined the SEP-363856-bound serotonin receptor (5-HT_{1A}R)–G_i-complex structure to further understand the polypharmacology for this anti-schizophrenic drug molecule. The structures of TAAR1 bound to METH and multiple ligands, including the endogenous biogenic amine β-PEA, provide essential insights into the molecular recognition and activation of TAAR1. Our findings may advance the understanding of the polypharmacology of the monoamine system and provide a valuable template for designing new ligands with improved therapeutic efficacy for treating neuropsychiatric disorders such as schizophrenia, depression and addiction.

Functional assessment of four TAAR1 agonists in activating TAAR1

The study of TAAR1 pharmacology has historically been challenging due to its low receptor expression and limited cell-surface availability, even in heterologous overexpression systems. Barak et al. employed the cAMP-based BRET (bioluminescence resonance energy transfer) biosensor to assess the activity of putative TAAR1 ligands³¹. Similarly, Svenningsson et al. provided evidence for the ability of SEP-363856 to activate TAAR1 at the surface plasma membrane through a G-protein recruitment assay system to study TAAR1 activation and G_s-dependent TAAR1 signalling³². Crystal methamphetamine is a synthetic drug that belongs to the amphetamine family; its primary active form, (S)-D-(+)-METH (to be named METH hereafter), is structurally similar to the endogenous amphetamine β-PEA and neurotransmitters such as dopamine (Fig. 1a). We first evaluated the potency of the four agonists METH, β-PEA, SEP-363856 and RO5256390 (Fig. 1a) in stimulating human TAAR1's G_s-signalling pathway through measurement of downstream cAMP accumulation (GloSensor assay, Methods). The results revealed that prominent G_s coupling resulted in a pEC₅₀ of 6.1, 7.1, 7.3, 7.7 for METH, SEP-363856, β-PEA and RO5256390, respectively (negative logarithm of the half-maximal effective concentration (pEC₅₀); averaged values from three independent experiments, Fig. 1b and Supplementary Tables 1 and 2). To validate the reliability of the functional data, the G_s heterotrimer recruitment assay^{32,33} and radioligand-binding assay were also performed to assess the potency of the four TAAR1 agonists (Extended Data Fig. 1 and Supplementary Tables 3 and 4). Remarkably, the ranking of agonist potency observed in these three assay systems—GloSensor, G_s recruitment assay and radioligand-binding assay—demonstrated remarkable consistency and alignment with previous studies^{7,32,34}. In particular, RO5256390 emerged as the most potent agonist, followed by β-PEA, SEP-363856 and METH. These results emphasize the accuracy and sensitivity of our functional assay in drawing substantive conclusions regarding TAAR1 pharmacology. Unless explicitly mentioned, all functional data in the subsequent study are obtained from the GloSensor experiment.

Overall structure of METH-activated TAAR1 complex

To investigate the molecular recognition of METH by TAAR1, we aimed to obtain a stable ligand-bound TAAR1–G_s complex for structural study. We first introduced a BRIL fusion (see Methods) at the N terminus of the human full-length TAAR1 for expression and purification³⁵. To improve the stability and homogeneity of the complex, we applied the NanoBiT tethering strategy³⁶. The TAAR1–G_s complex was formed by co-expressing TAAR1 with a dominant-negative form of human Gα_s containing two mutations (G226A and A366S)³⁷, rat Gβ₁ and bovine Gγ₂ in SF9 insect cells. During purification, a single-chain antibody, Nb35, was added to stabilize the nucleotide-free TAAR1–G_s complexes³⁸ (Extended Data Fig. 2). The purified TAAR1–G_s complex was further analysed by single-particle cryo-EM to determine its structure.

The structure of the METH-bound TAAR1–G_s complex was determined with a global resolution of 2.8 Å (Fig. 1c, Extended Data Fig. 2 and Extended Data Table 1). The high-resolution density map allowed us to model most portions of TAAR1, the ligand molecule, the G_s heterotrimer and Nb35 (Fig. 1c,d and Extended Data Fig. 2). The overall structure of TAAR1 consists of a canonical transmembrane domain of seven transmembrane helices (TM1–TM7), all three extracellular loops 1–3 (ECL1–ECL3), a short intracellular loop 2 (ICL2) helix, and an amphipathic helix, H8. Notably, ECL2 forms an additional helix folded over the cap of the ligand-binding pocket, a characteristic that has been frequently observed in classical aminergic receptors. However, the precise configuration of ECL2 in TAAR1 exhibits the greatest resemblance to that observed in β₂AR and 5-HT₄R (Fig. 1d and Extended Data Fig. 1).

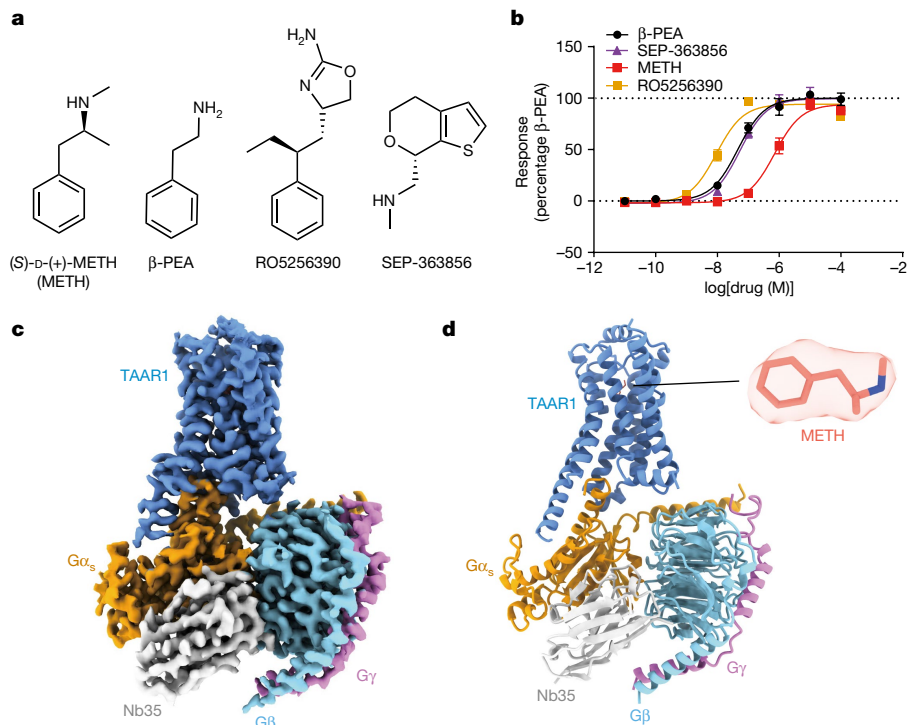


Fig. 1 | Functional assessment of four TAAR1 agonists in activating TAAR1 and overall structure of METH-TAAR1-G_s complex. **a**, Chemical formula of METH, β-PEA, SEP-363856 and RO5256390. **b**, Concentration–response curves of the four agonists in activating TAAR1 by measuring the cellular cAMP

accumulation through the GloSensor assay. Data are mean ± s.e.m. from three independent experiments ($n = 3$). **c,d**, Cryo-EM density map (**c**) and cartoon presentation (**d**) of the METH-TAAR1-G_s complex. The complex density map is shown at a contour level of 0.15.

The binding mode of METH in TAAR1

In our METH-TAAR1-G_s complex structure, METH occupies the orthosteric binding pocket of TAAR1, which is lined by the transmembrane helices 3, 5, 6 and 7 (Fig. 2a) and is capped by ECL2 loop (ECL2_{loop}, residues 180–186) and the upper part of ECL2 helix (ECL2_{helix}, residues 175–179) (Fig. 1d and Fig. 2a).

Overall, the recognition of METH by TAAR1 is primarily based on its two chemical moieties: a phenylpropyl group and an amino-methyl group (Fig. 2a,b). The most prominent interaction is a polar interaction between the secondary amine in the amino-methyl group and TAAR1 residue D103^{3x32} (generic residue numbers from GPCRdb in superscript)³⁹ (Fig. 2b,c), a common interaction mode shared by all known aminergic receptors, including serotonin receptors and dopamine receptors^{33,40}. Moreover, D103^{3x32} ranks among the top predicted binding sites for TAAR1-ligand interactions based on prior modelling analyses^{41–44}. In TAAR1, D103^{3x32} is further stabilized by forming direct hydrogen bonds with Y294^{7x43} and H99^{3x28}. Additionally, Y294^{7x43} forms a hydrogen bond with S80^{2x61}, resulting in the establishment of a hydrogen-bonding network consisting of the residues D103^{3x32}, Y294^{7x43}, S80^{2x61}, R83^{2x64} and H99^{3x28} (Fig. 2b,c). Previous studies showed that residue at position 3x28 plays a key role in drug recognition and selectivity of 5-HT₄R (ref. 45), so does the residue at position 2x64 in β₁AR (ref. 46), suggesting that such a hydrogen-bonding network, formed by residues in positions 3x28 and 2x64 tethered with residues at positions 3x32 and 7x43, may play important roles in drug recognition and selectivity for aminergic receptors. The secondary amine in the amino-methyl group also forms a hydrogen bond with S107^{3x36}, which stabilizes the ligand binding in the TAAR1 pocket. The phenylpropyl group of METH forms hydrophobic contacts with hydrophobic residues that constitute the binding pocket, including I104^{3x33}, V184^{45x52}, F186^{45x54}, T194^{5x42}, W264^{6x48}, F267^{6x51} and F268^{6x52} (Fig. 2d). Meanwhile, the methyl group (m1) from the propenyl end is directed to the hydrophobic subpocket formed by F267^{6x51}, I290^{7x39}

and W264^{6x48} (Fig. 2e). Additionally, the other methyl group (m2) located at the end of the amino-methyl group finds a snug fit within the hydrophobic environment, encompassed by I290^{7x39} and V184^{45x52} (Fig. 2e).

To gain insight into the recognition of METH by TAAR1, we carried out mutagenesis studies on the key interacting residues using the GloSensor assay to measure cAMP accumulation stimulated by agonist binding. The result showed alanine substitution of D103^{3x32} or Y294^{7x43} almost abolished the activation of TAAR1 by METH. Disrupting the hydrogen bond between METH and S107^{3x36} also greatly reduced TAAR1 activation (Fig. 2f and Supplementary Table 1). Surprisingly, mutating residues from the hydrogen-bonding network had a profound impact on activation of TAAR1 by METH. H99^{3x28}A and R83^{2x64}A mutations almost abolished the activation of TAAR1, while S80^{2x61}A reduced the maximum activation to about 50% of that of wild type (Fig. 2f and Supplementary Table 1), indicating the importance of the hydrogen-bonding network in METH recognition by TAAR1. Mutations of surrounding residues that form hydrophobic interactions with METH also have a variable effect on the activation of TAAR1 by METH. Alanine substitution of I104^{3x33}, F186^{45x54} and W264^{6x48} almost abolished the activation of TAAR1 by METH, and F267^{6x51}A caused a 100-fold potency decrease in TAAR1 activation accompanied by about 38% of maximum activation to that of wild type. Besides, I290^{7x39}A, V184^{45x52}A and F268^{6x52}A induce about 10-fold potency decrease in TAAR1 activation (Fig. 2g and Supplementary Table 1). Our structural findings were reinforced by subjecting these mutants to a secondary functional assay, which measured G_s recruitment upon agonist activation (Extended Data Fig. 3 and Supplementary Table 3). Together, these results validate the molecular mechanism of METH recognition by TAAR1.

The binding mode of β-PEA

β-PEA and METH share common phenyl motifs, with METH having two additional methyl groups compared with β-PEA (Fig. 1a). To investigate

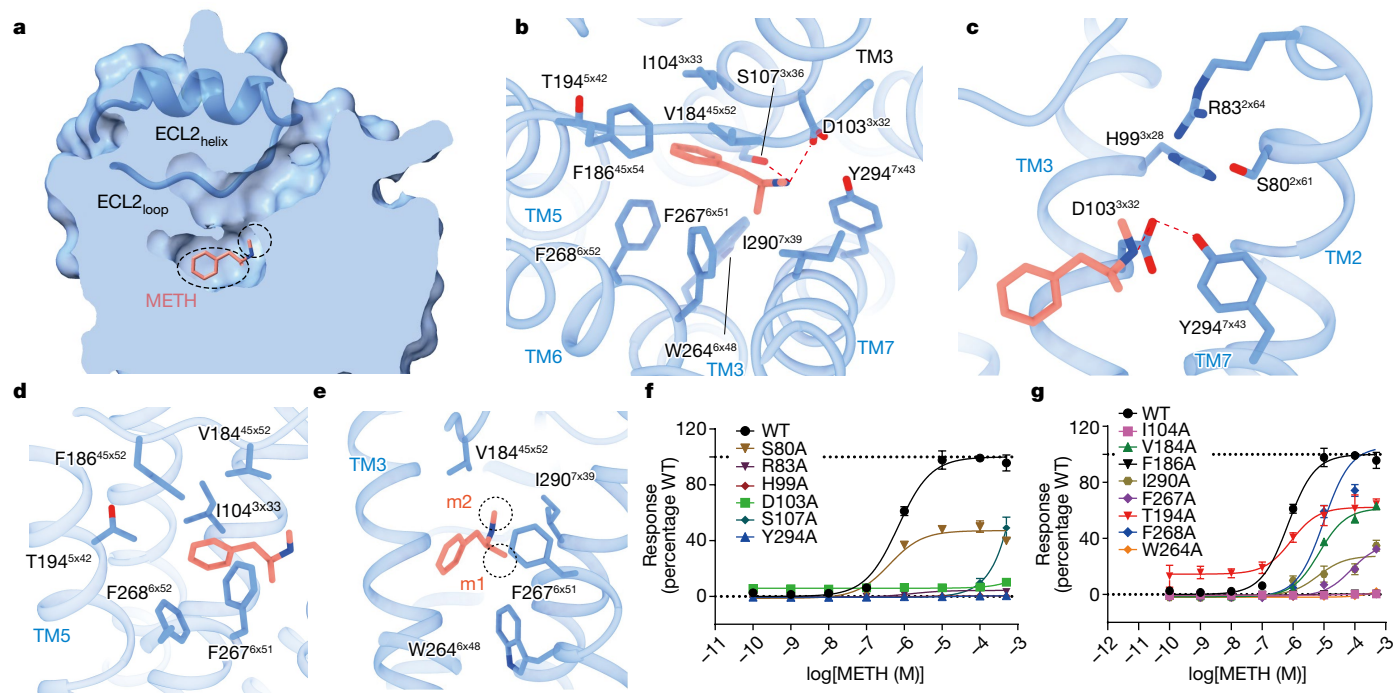


Fig. 2 | METH-binding pocket of TAAR1. **a**, Cross-section of the METH-binding pocket in TAAR1. The two chemical moieties of METH are highlighted in the black-dotted circles. **b**, Molecular interactions between METH and residues from TAAR1. **c**, Key polar interactions between the primary amine in amino-methyl group of METH and D103^{3x32} in TAAR1. The hydrogen-bonding network to stabilize the interaction is also shown. **d**, The non-polar interactions between

the phenylpropyl group of METH and residues from TAAR1. **e**, The two methyl groups of METH are directed to the hydrophobic subpocket formed by V184^{45x52}, F267^{6x51}, I290^{7x39} and W264^{6x48}. **f,g**, Effects of mutating TAAR1 on the polar interactions (**f**) and hydrophobic interactions (**g**) within the METH-binding pocket. Data are mean \pm s.e.m. from three independent experiments ($n=3$).

the binding mode of β -PEA in TAAR1, we obtained the structure of the β -PEA-activated TAAR1-G_s complex with an overall resolution of 3.0 Å (Extended Data Fig. 2 and Extended Data Table 1). Similar to METH, β -PEA occupies the orthosteric binding pocket of TAAR1 (Fig. 3a) and is stabilized by polar interactions and a hydrogen-bonding network involving D103^{3x32}, Y294^{7x43}, S107^{3x36}, H99^{3x28}, R83^{2x64} and S80^{2x61} (Figs. 2c and 3b). Additionally, the phenyl group of β -PEA forms extensive hydrophobic interactions with surrounding residues, including F186^{45x54}, T194^{5x42}, W264^{6x48}, F267^{6x51} and F268^{6x52} (Fig. 3b).

To validate the β -PEA binding mode observed in the structure, we performed GloSensor assay for wild type and TAAR1 mutants in the presence of β -PEA. Among them, mutations of the conserved D103^{3x32} and Y294^{7x43}, both of which form a polar interaction network with the amine group of β -PEA, completely abolishing the ability of β -PEA to activate TAAR1 (Fig. 3c). Additionally, mutations of residues in the binding pocket that directly interact with β -PEA, including S107^{3x36}A, F186^{45x54}A, F186^{45x54}W, F267^{6x51}A, F268^{6x52}A, T194^{5x42}A, and W264^{6x48}A, all displayed loss of cAMP production when compared to WT TAAR1 (Fig. 3d). Furthermore, mutations of the hydrogen-bonding network residues that contribute to the interaction with β -PEA, such as H99^{3x28}A, R83^{2x64}A, and S80^{2x61}A, also reduced activities of β -PEA in activating TAAR1 consistent with that of METH (Fig. 3e, Extended Data Fig. 3 and Supplementary Tables 1 and 3).

Our functional data indicate that β -PEA is over 10 times more potent than METH in activating TAAR1 (Fig. 1b). Structural comparison of the METH and β -PEA binding pockets in TAAR1 unveils a notable distinction that may account for the higher potency of β -PEA. Notably, β -PEA forms shorter-distance polar interactions with D103^{3x32} and hydrogen bonding with S107^{3x36} compared with the interactions METH forms with those same residues in the METH-bound TAAR1 structure. This difference could be attributed to the orientation of the two additional methyl groups in METH, which direct towards V184 of ECL2 and the

hydrophobic subpocket constituted by V184^{45x52}, I290^{7x39}, F267^{6x51} and W264^{6x48}, possibly causing an upward shift of METH's secondary amine group (Fig. 3e). In addition, Y294^{7x43} interacts directly with β -PEA but not with METH, which further stabilizes the binding of β -PEA in the TAAR1 pocket. Taken together, these structural differences may account for the difference in potency between β -PEA and METH in activating TAAR1.

To gain deeper insights into the disparity in potency between β -PEA and METH in activating TAAR1, molecular dynamic simulations were conducted. Analysing the root-mean-square deviation (RMSD) plots derived from molecular dynamic simulations of the representative test set reveals a noticeable difference: β -PEA exhibits greater stability within the TAAR1 pocket throughout the simulation period compared with METH (Extended Data Fig. 3). The binding free energy decomposition analysis reveals that D103^{3x32}, S107^{3x36} and Y294^{7x43} contribute to the stability of β -PEA binding to TAAR1. As such, these residues emerge as potential key determinants responsible for the higher potency of β -PEA relative to METH (Extended Data Fig. 3). These results are consistent with our structural analysis and mutagenesis data.

Structural basis of SEP-363856 polypharmacology

SEP-363856 is a promising anti-schizophrenic drug candidate in the treatment of schizophrenia and other psychotic disorders. It has been found to activate TAAR1 and 5-HT_{1A}R receptors with different potency^{7,32}. To better understand the structural basis of SEP-363856's dual agonist activity, we determined the structures of TAAR1 and 5-HT_{1A}R bound to SEP-363856, each at a global resolution of 2.6 Å and 3.0 Å, respectively (Fig. 4a,b, Extended Data Fig. 4 and Extended Data Table 1).

In the structures of TAAR1 or 5-HT_{1A}R complexes, SEP-363856 is found in the same orthosteric pocket and adopts a similar L-shaped binding pose (Extended Data Fig. 5). In both structures, the

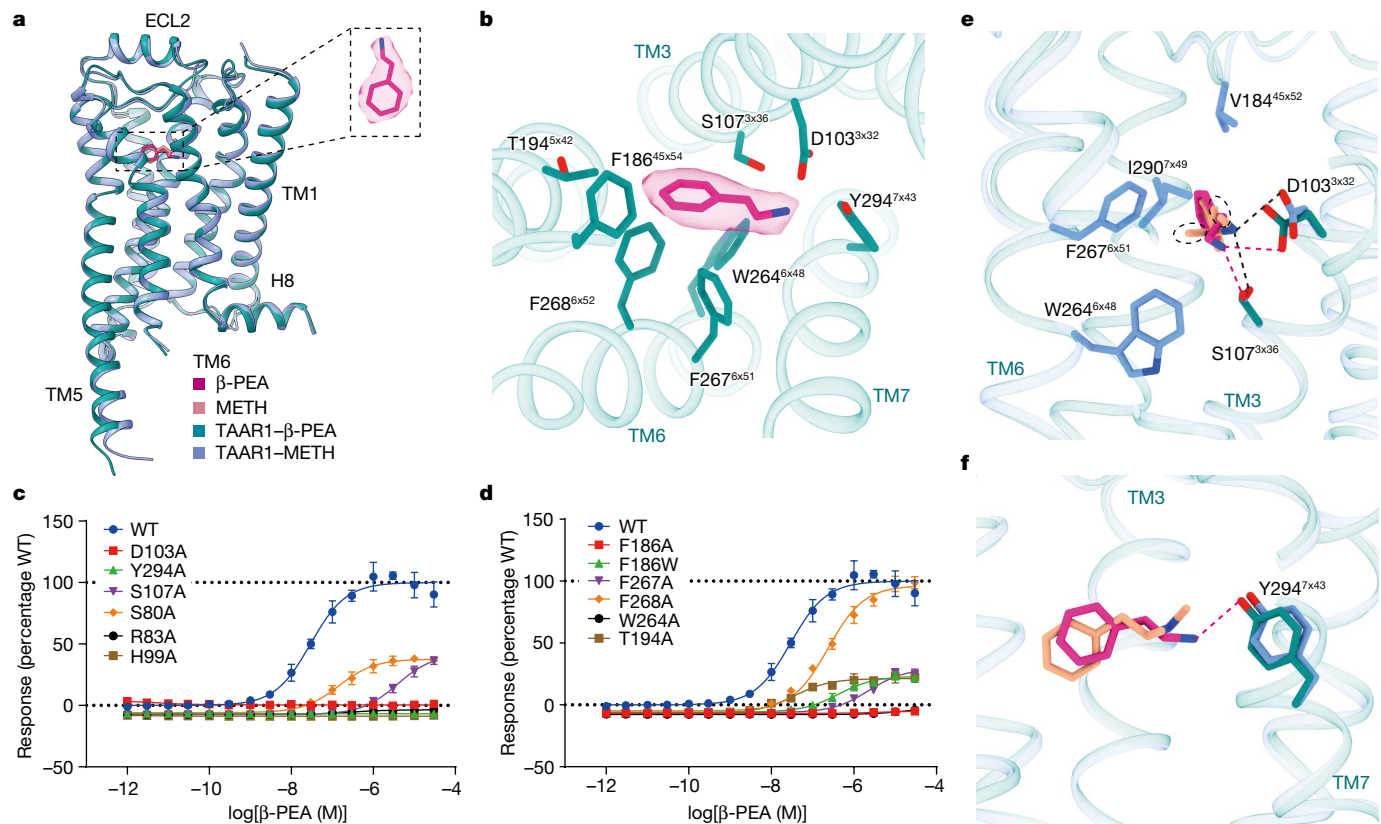


Fig. 3 | The recognition of β-PEA by TAAR1. **a**, Structural comparison of β-PEA and METH-activated TAAR1 structures, β-PEA in the binding pocket is highlighted in the dotted box. **b**, Molecular interactions between β-PEA and key residues from TAAR1. **c,d**, Concentration–response curves for point mutations of key residues in TAAR1 related to polar interaction network (**c**) and hydrophobic interactions (**d**), induced by β-PEA using GloSensor assay. Data are mean \pm s.e.m.

from three independent experiments ($n=3$). **e**, Comparison of the key molecular interactions between the two ligands, β-PEA (red-dotted line) and METH (black-dotted line), with D103 and S107 in TAAR1. The two methyl group of METH compared to β-PEA is highlighted in the black-dotted cycle. **f**, Direct interaction between Y294^{7x43} and β-PEA, absent in METH.

N-methylmethanamine group of SEP-363856 orients toward TM3 and TM6, with its positively charged N atom forming a salt bridge with the sidechain of D^{3x32} in TM3, which is further stabilized by Y^{7x43} (Fig. 4c,d). The thienopyran moiety of SEP-363856 occupies a region of binding pocket contributed by residues from TM3 and TM6, and interacts with surrounding residues including 3x33, 3x36, 45x52, 45x54, 6x48, 6x51 and 6x52 in TAAR1 and 3x33, 3x36, 3x37, 45x52, 5x46, 6x48, 6x51 and 6x52 in 5-HT_{1A}R (Fig. 4c,d). The conserved residue D^{3x32} is critical to ligand binding for 5-HT and other monoamine receptors, by forming a conserved salt bridge with the basic cyclic amine of ligands^{33,40,45,47,48}. Residues at positions 3x32, 6x48, 6x51, 6x52 and 7x43 are conserved across the two receptors and are known to determine ligand recognition by 5-HT_{1A}R (ref. 33) (Extended Data Fig. 5). The common interactions that govern the recognition of SEP-363856 by TAAR1 or 5-HT_{1A}R may provide the structural foundation for the polypharmacology of SEP-363856.

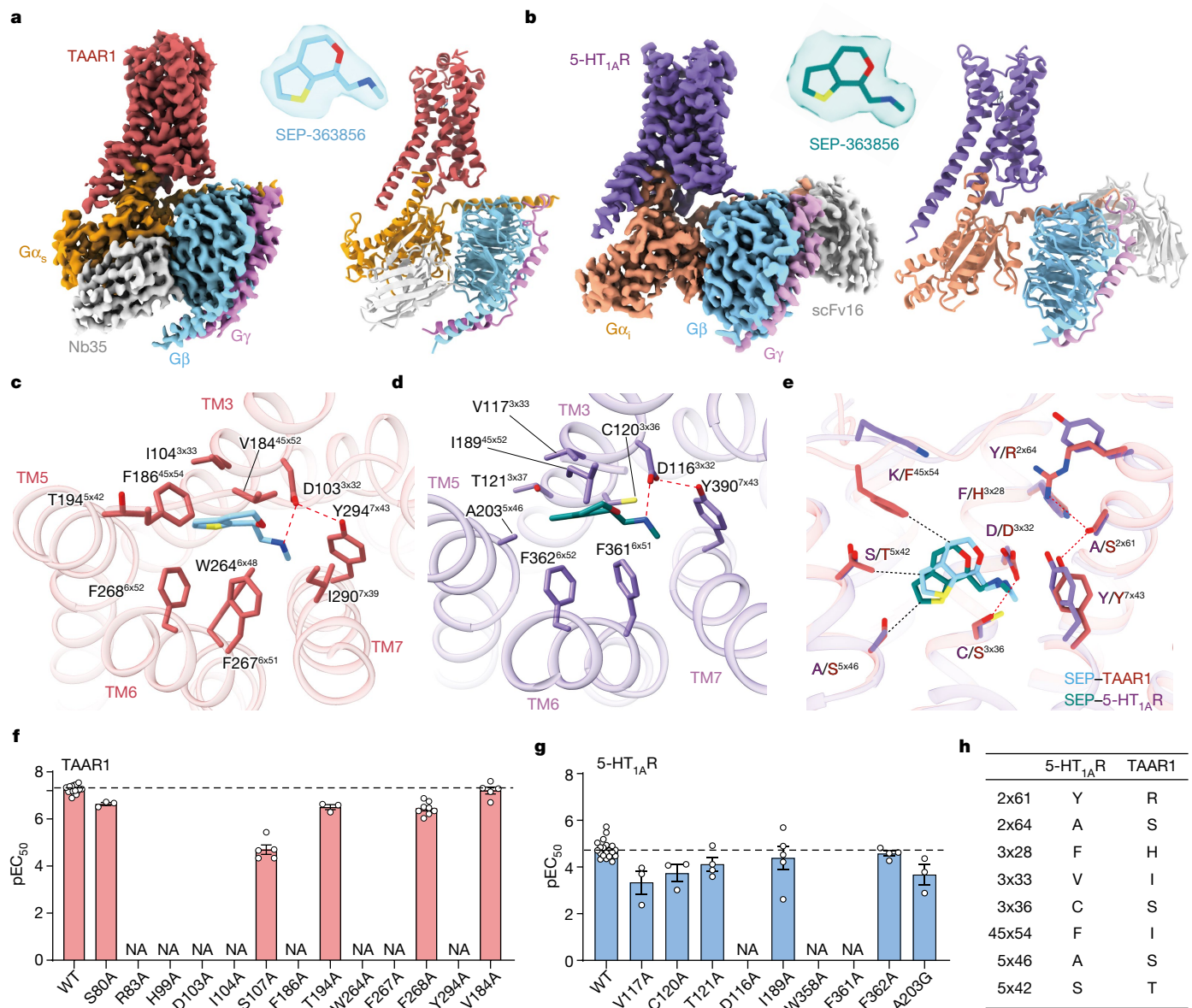
Additionally, there are notable differences in the molecular contacts between SEP-363856 and the two receptors. In TAAR1, the salt bridge between the positively charged N atom and sidechain of D^{3x32} is further stabilized by a hydrophilic network consisting of S107^{3x36}, H99^{3x28}, S80^{2x61} and R83^{2x64}, as observed in the β-PEA-bound TAAR1 structure, which is absent in the 5-HT_{1A}R structure (Fig. 4e). Additional contacts between the thienopyran moiety of SEP-363856 and F186^{45x54} and T194^{5x42} are observed in TAAR1 but not in the 5-HT_{1A}R structure (Fig. 4e). Furthermore, the alanine at position 5x46 in 5-HT_{1A}R forms a hydrophobic interaction with SEP-363856, which cannot be formed by the corresponding serine residue S198 in TAAR1 (Fig. 4e). These differences in the specific interactions between SEP-363856 and the

two receptors may account for the 100-fold higher activation potency of SEP-363856 for TAAR1 compared with 5-HT_{1A}R (Fig. 4f,g). The key interactions determining the potency and selectivity of SEP-363856 for TAAR1 and 5-HT_{1A}R receptors were validated through a combination of functional assays and sequence alignments (Fig. 4f–h, Extended Data Fig. 3 and Supplementary Tables 2, 4 and 5).

Molecular mechanism of the high potency and selectivity of RO5256390

RO5256390, composed of phenyl–butyl and oxazol-2-ylamine moieties, is a selective and sub-nanomolar potent agonist for TAAR1. To elucidate the high-potency binding mode of RO5256390 for TAAR1, we obtained the structure of the RO5256390-activated TAAR1-G_s complex with an overall resolution of 2.8 Å (Fig. 5a, Extended Data Fig. 5 and Extended Data Table 1). In the RO5256390-TAAR1 structure, RO5256390 adopts a ‘l’-shape configuration within the binding pocket, with the methyl group of phenyl–butyl extending toward ECL2, and the oxazol-2-ylamine moiety inserted into the cavity formed by D103^{3x32}, S107^{3x36}, W264^{6x48} and Y294^{7x43} (Extended Data Fig. 6). The key residues crucial for the recognition of RO5256390 by TAAR1 were validated through mutagenesis and functional data (Fig. 5b, Extended Data Figs. 3 and 6 and Supplementary Tables 2 and 4).

Among the four TAAR1 agonists, RO5256390 emerges as the most potent one, establishing an extensive network of contacts with residues located within the TAAR1 pocket. Investigation of the RO5256390-activated TAAR1 structure reveals that several interactions likely play pivotal roles in augmenting its potency: a hydrophobic interaction

**Fig. 4 | Structural basis of SEP-363856 polypharmacology and selectivity.**

a,b, Cryo-EM density map and cartoon presentation of SEP-363856 bound TAAR1-G α _s (**a**) or 5-HT_{1A}R-G α _i (**b**) complex structures. Both complex density maps are shown at contour level of 0.15. **c,d**, Molecular interactions between SEP-363856 and residues from TAAR1 (**c**) or 5-HT_{1A}R (**d**). **e**, Comparison of key differences in SEP-363856 interactions with TAAR1 and 5-HT_{1A}R. The red-dotted line shows interactions only present in TAAR1, and the black-dotted line shows

interactions only present in 5-HT_{1A}R. **f,g**, Effects of mutations of residues in TAAR1 (**f**) or 5-HT_{1A}R (**g**) in the SEP-363856 binding pocket using GloSensor assay. pEC₅₀ represents calculated potency for SEP-363856 on each mutant. NA (not activated) indicates that the value cannot be fitted by non-linear regression in GraphPad Prism. Data are mean \pm s.e.m. from three independent experiments ($n=3$). **h**, Sequence comparison of interacting residues between TAAR1 and 5-HT_{1A}R with variation.

between the phenyl-butyl group with V184^{45x52} and I290^{7x39}, a pi-pi interaction involving the oxazol ring and Y294^{7x43}, and the formation of a hydrogen bond facilitated by the 2-ylamine and S107^{3x36} (Fig. 5b and Extended Data Fig. 6).

To confirm the selectivity of RO5256390 for TAAR1 over 5-HT_{1A}R, we conducted activation tests on both receptors using RO5256390 (Fig. 1b, Extended Data Fig. 6 and Supplementary Tables 2 and 4). The results clearly demonstrate that RO5256390's activation of the 5-HT_{1A}R is notably less potent than that of TAAR1. Additionally, the maximal activation achieved through RO5256390's interaction with the 5-HT_{1A}R is substantially reduced (only 23% of the response observed with 5-HT) (Extended Data Fig. 6). This outcome strongly suggests that the efficacy of RO5256390 in activating the 5-HT_{1A}R is markedly limited. To clarify this selectivity from a structural perspective, we manually docked

RO5256390 into the SEP-363856-activated 5-HT_{1A}R structure. Structural analysis revealed that the serine residue in the 3x36 position of TAAR1 forms a hydrogen bond with the amino group of the oxazol-2-ylamine moiety of RO5256390 (Fig. 5c and Extended Data Fig. 6), whereas the corresponding residue in the 5-HT_{1A}R is cysteine, which cannot form a hydrogen bond but instead causes a potential clash with the amino group in the ligand (Fig. 5c). The 3x36 residue is reported to be important for ligand selectivity in 5-HTRs (refs. 33,45,47,48). Functional data indicated that alanine substitution of S107^{3x36} decreased potency of RO5256390 in activating TAAR1 by about 10-fold, accompanied by a nearly 50% reduction of the maximum activation as that of wild type, while the cysteine substitution almost abolished the activation of TAAR1 (Fig. 5d). In contrast, the 5-HT_{1A}R with an alanine substitution at position C120^{3x36} displayed a weak response to RO5256390. Interestingly,

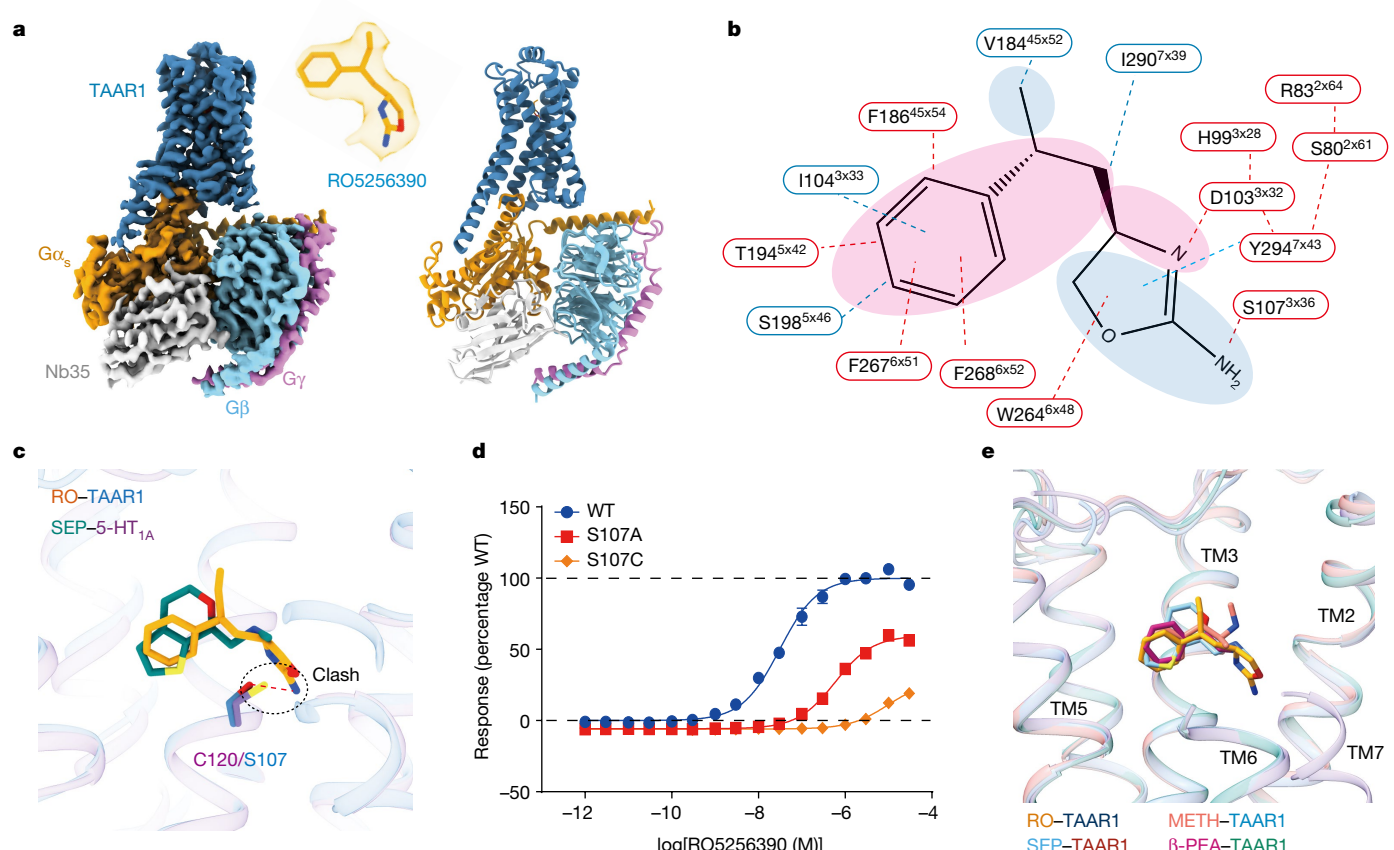


Fig. 5 | Conserved and divergent features of agonist recognition at TAAR1. **a**, Cryo-EM density map and cartoon presentation of RO5256390-activated TAAR1- G_s structure. The complex density map is shown at a contour level of 0.15. **b**, Diagram of RO5256390 interacting residues, the background indicated two moieties of RO5256390, the residues and dotted line in red colour represent common interactions, that in blue colour represent residues specific for RO5256390 recognition by TAAR1. **c**, Superposition of RO5256390-activated TAAR1 with SEP-363856 activated 5-HT_{1A}R structures to show the model of RO5256390 in 5-HT_{1A}R. The black-dotted circle shows potential clash between RO5256390 and C120^{3x36} in 5-HT_{1A}R. Red-dotted line indicates the interaction between RO5256390 and S107^{3x36} of TAAR1. **d**, Validation of S107^{3x36} in determining selectivity of RO5256390. Concentration-response curves for this residue mutation on TAAR1 induced by RO5256390 using GloSensor assay. Data are mean \pm s.e.m. from three independent experiments ($n = 3$). **e**, Superposition of the four ligand-binding pockets in TAAR1. **f**, List of key residues in TAAR1 binding pockets for the four ligands (METH, β -PEA, SEP-363856, RO5256390). Residues in green background represent common interactions for the four ligands.

RO5256390 and C120^{3x36} in 5-HT_{1A}R. Red-dotted line indicates the interaction between RO5256390 and S107^{3x36} of TAAR1. **d**, Validation of S107^{3x36} in determining selectivity of RO5256390. Concentration-response curves for this residue mutation on TAAR1 induced by RO5256390 using GloSensor assay. Data are mean \pm s.e.m. from three independent experiments ($n = 3$). **e**, Superposition of the four ligand-binding pockets in TAAR1. **f**, List of key residues in TAAR1 binding pockets for the four ligands (METH, β -PEA, SEP-363856, RO5256390). Residues in green background represent common interactions for the four ligands.

when the serine substitution was introduced at position C120^{3x36} in the 5-HT_{1A}R, the efficacy of RO5256390 was restored. In this scenario, the maximum activation achieved by RO5256390 was approximately 120% of the response obtained with 5-HT activation at the 5-HT_{1A}R, although the potency remained relatively low (Extended Data Fig. 6). The above results were cross-validated in other assay systems by assessing the $G\alpha_i\beta\gamma$ dissociation assay (see Methods) for 5-HT_{1A}R activation (Extended Data Fig. 6), or G_s recruitment for TAAR1 activation (Extended Data Fig. 3). Taken together, we concluded that S107^{3x36} in TAAR1 may play a key role in determining selectivity of RO5256390 for TAAR1.

The common structural features in TAAR1 agonist recognition

The comparison of the four TAAR1 structures reveals that the overall structures of TAAR1 bound to the four agonists are highly similar, with RMSD values of 0.403 Å, 0.387 Å, 0.328 Å for the Cα atoms of TAAR1 when comparing the METH, SEP-363856, RO5256390-activated TAAR1 structures with that activated by β -PEA, respectively. In all four TAAR1 structures, TAAR1 displays a canonically activated conformation, with all ligands located at the orthosteric binding site in similar poses (Fig. 5e).

Article

Notably, in all four structures, ECL2 forms a loop ($\text{ECL2}_{\text{loop}}$) covering the ligand-binding pocket, where the F186^{45x54} and V184^{45x52} shape the top pocket of TAAR1 and participate in hydrophobic interactions with the ligand. Mutations of F186A almost abolished TAAR1 activation by all four ligands (Figs. 2g, 3d and 4f and Extended Data Fig. 6), while V184A mutation also reduced TAAR1 activation substantially (Figs. 2g, and 4f and Extended Data Fig. 6), which indicated the important role of F186^{45x54} and V184^{45x52} in ligand binding and TAAR1 activation. The $\text{ECL2}_{\text{loop}}$ structure shares consensus in configuration with other aminergic receptors, except for the 45x54 position, which is highly divergent (Extended Data Fig. 7a). In structures of other aminergic receptors, especially in 5-HT_{Rs}, dopamine receptors and adrenoceptor family, the residues at 45x54 are varied (Extended Data Fig. 7b). In TAAR1, F186^{45x54} and V184^{45x52} restrict the size of the orthosteric pocket, resulting in a more compact binding pocket to accommodate smaller ligands in a restricted conformation. Together, the $\text{ECL2}_{\text{loop}}$, including the highly divergent F186^{45x54} , may shape the pocket of TAAR1 to accommodate a range of trace amines in the brain. The role of F186^{45x54} in drug recognition and selectivity in TAAR1 merits further investigation.

Further detailed structural analysis revealed a common structural basis for the ligand recognition by TAAR1. The common interactions between TAAR1 and the four different ligands include: (1) the salt bridge formed between D103^{3x32} and the cationic N atom in the ligand, which is further stabilized by a hydrogen-bonding network involving Y294^{7x43}, R83^{2x64}, H99^{3x28} and S80^{2x61}; (2) the hydrophobic or $\pi-\pi$ stack formed by alkyl-substituted aromatic rings in the ligand with surrounding residues, including F186^{45x54} , W264^{6x48}, F267^{6x51} and F268^{6x52}, among which the F186^{45x54} on ECL2 is the least conserved pocket-forming residue within the aminergic receptor family (Extended Data Fig. 7); (3) the hydrogen bond formed by S107^{3x36} in TAAR1, which interacts with the cationic N atom from the ligands or the sidechain of D103^{3x32}. These interactions provide a framework for the ligand recognition by TAAR1 (Fig. 5f and Extended Data Fig. 6).

We next explored the ligand selectivity of TAAR1 agonists in the broader context of the TAAR family. Previous studies indicated that no functional responses to β -PEA were found in COS-7 cells expressing other human TAAR subtypes⁴⁹. With this knowledge in mind, we proceeded to evaluate the capacity of the four ligands— β -PEA, METH, RO5256390, and SEP-363856—in activating other TAAR subtypes. Our investigations revealed that the remaining five human TAARs (hTAAR2/5/6/8/9) failed to respond to activation by the above four ligands as determined by GloSensor assays (Extended Data Fig. 8). Through further sequence alignment and structural analysis (Extended Data Fig. 9), we found that although positions like 3x32, 6x48 and 7x43, responsible for recognizing amines in the ligands, are conserved across the hTAAR family, other pocket residues crucial for TAAR1 agonist recognition—including 3x36 and 6x51—are not conserved in other hTAARs. The divergence in these key residues might contribute to the TAAR1 selectivity observed in the ligands tested.

Mechanism of TAAR1 activation

Given the nature of TAAR1 in recognizing biogenic amines, we next compared its activation mechanism with that of other aminergic receptors, particularly 5-HT₄R and β_2 AR, which exhibit the highest sequence homology to TAAR1. The comparison indicated that the four structures of TAAR1–G_s-signalling complexes are all in active states⁵⁰ (Extended Data Fig. 9). Structural alignment of the active β -PEA-bound TAAR1 to the inactive β_2 AR structure indicated the conformational changes of TAAR1 at both cytoplasmic and extracellular regions^{51,52} (Extended Data Fig. 9). Specifically, the binding of β -PEA induced a downward shift in the toggle switch residue W264^{6x48} within TAAR1 (Extended Data Fig. 9). This shift in W^{6x48} was accompanied by alterations in the conformations of residue F^{6x44} in the P^{5x50}I^{3x40}F^{6x44} motif, R^{3x50} in the D^{3x49}R^{3x50}Y^{3x51} motif, and an inward shift of TM7 (Extended Data Fig. 9). These conformational

adjustments corresponded with the disruption of the conserved ionic lock between R^{3x50} and D^{6x30}, as well as an outward movement of approximately 9 Å at the cytoplasmic end of TM6 (Extended Data Fig. 9). Collectively, these findings underscore that the activation mechanism of TAAR1 aligns with the classical aminergic GPCRs.

Discussion

METH is a psychostimulant that was originally used to treat obesity and attention deficit hyperactivity disorder (ADHD) but is abused recreationally, becoming a threat to human health and society. The molecular mechanism underlying METH recognition by TAAR1 has garnered substantial attention, given its profound connection with METH signalling. This process intricately involves other biological pathways, including DAT, VMAT and other players, collectively contributing to the complex development of METH addiction. In our study, we provide structural insights into METH recognition by TAAR1, elucidate key determinants essential for METH activation and uncover the unique structural features of TAAR1. By comparing structures of TAAR1 bound to different ligands, including the endogenous ligand β -PEA, METH and two drug candidates, we demonstrate the common ligand-binding mode in the orthosteric binding pocket of TAAR1 as well as the key residues involved in contributing to the ligand selectivity.

TAAR1 has emerged as a promising therapeutic target for the treatment of addiction and neuropsychiatric disorders, including schizophrenia. SEP-363856, a TAAR1 and 5-HT_{1A}R dual agonist, is currently in clinical trials for the treatment of schizophrenia. Structural comparison of SEP-363856-activated TAAR1 and 5-HT_{1A}R structures provides insights into the structural basis for polypharmacology of SEP-363856, with conserved key residues at positions 3x32, 6x51, 6x52 and 7x43 in the binding pocket contributing to its dual agonism. The insights gained from these structural features can serve as a valuable foundation for designing new ligands with enhanced therapeutic potential in treating neuropsychiatric conditions such as drug addiction, relapse and schizophrenia. It is noteworthy that while understanding the structural basis of TAAR1 activation aligns with the ongoing efforts in TAAR1-targeted drug discovery, TAAR1 antagonists may also present values for comprehensive understanding of TAAR1 pharmacology and thus warrant future investigations^{53,54}.

TAAR1 shares sequence similarity ranging from 39% to 50% with other TAAR family members, which are also referred to as olfactory TAARs. Our study strongly indicates that the four agonists examined in this research exhibit exclusive activation of TAAR1 in our functional assay system, signifying a distinct TAAR1-selective binding pattern. Interestingly, various motifs associated with the activation of class A GPCR—including the toggle switch (W^{6x48}, P^{5x50}I^{3x40}F^{6x44} motif, D^{3x49}R^{3x50}Y^{3x51} motif and N^{7x49}P^{5x50}XXY^{7x53} motif)—are conserved among the TAAR family (Extended Data Fig. 9). Moreover, a side-by-side comparison of hTAAR1 with the recently reported mTAAR9 structure⁵⁵ unveils a strikingly similar activation mechanism: notably, the cytoplasmic end of TM6 in both receptors exhibited an outward shift to accommodate the Gproteins. Moreover, the conventional W^{6x48} toggle switch within both hTAAR1 and mTAAR9 established a direct interaction with the ligands, inducing a downward movement of the W^{6x48} toggle switch. The conformational changes in the conserved microswitches, including W^{6x48} and F^{6x44}, and the packing changes between TM3 and TM6, are potential shared mechanisms in mediating the activation of hTAAR1 and mTAAR9 (Extended Data Fig. 9). These analyses imply that olfactory TAARs may share a common activation mechanism with hTAAR1.

Previous literature indicates the species-dependent selectivity of TAAR1 for its ligands, with METH demonstrating higher potency for mouse and rat TAAR1 compared with human TAAR1 (ref. 34). Despite the conservation of key residues in the ligand-binding pocket across the three species (Extended Data Fig. 9), our molecular dynamics simulations reveal distinct stability patterns in METH binding among

them. Notably, lower RMSD values for METH binding in mouse and rat TAAR1 binding pockets stand in contrast with human TAAR1 (Extended Data Fig. 9). This differential stability in binding interactions, as indicated by RMSD profiles, provides valuable insight into molecular dynamics and potential structural dynamics that might contribute to the observed potency differences between species. The comprehension of the molecular foundation underlying species-specific interactions undoubtedly holds notable implications for the development of both TAAR1 agonists and antagonists. While several studies have delved into the molecular mechanism^{41,44}, additional research is essential to achieve a comprehensive understanding of the factors that dictate species selectivity of TAAR1-ligand interactions.

Online content

Any methods, additional references, Nature Portfolio reporting summaries, source data, extended data, supplementary information, acknowledgements, peer review information; details of author contributions and competing interests; and statements of data and code availability are available at <https://doi.org/10.1038/s41586-023-06775-1>.

1. Gainetdinov, R. R., Hoener, M. C. & Berry, M. D. Trace amines and their receptors. *Pharmacol. Rev.* **70**, 549–620 (2018).
2. Liu, J., Wu, R. & Li, J.-X. TAAR1 and psychostimulant addiction. *Cell. Mol. Neurobiol.* **40**, 229–238 (2020).
3. Most overdose deaths involve illicitly manufactured fentanyl. CDC www.cdc.gov/drugoverdose/featured-topics/overdose-deaths-data.html (2020).
4. Berry, M. D., Gainetdinov, R. R., Hoener, M. C. & Shahid, M. Pharmacology of human trace amine-associated receptors: therapeutic opportunities and challenges. *Pharmacol. Ther.* **180**, 161–180 (2017).
5. Dodd, S. et al. Trace amine-associated receptor 1 (TAAR1): a new drug target for psychiatry? *Neurosci. Biobehav. Rev.* **120**, 537–541 (2021).
6. Heffernan, M. L. R. et al. Ulotorant: A TAAR1 agonist for the treatment of schizophrenia. *ACS Med. Chem. Lett.* **13**, 92–98 (2022).
7. Nair, P. C. et al. Binding of SEP-363856 within TAAR1 and the 5HT1A receptor: implications for the design of novel antipsychotic drugs. *Mol. Psychiatry* **27**, 88–94 (2022).
8. Schep, L. J., Slaughter, R. J. & Beasley, D. M. The clinical toxicology of metamfetamine. *Clin. Toxicol.* **48**, 675–694 (2010).
9. Jayanthi, S., Daiwile, A. P. & Cadet, J. L. Neurotoxicity of methamphetamine: main effects and mechanisms. *Exp. Neurol.* **344**, 113795 (2021).
10. Chan, B. et al. Pharmacotherapy for methamphetamine/amphetamine use disorder—a systematic review and meta-analysis. *Addiction* **114**, 2122–2136 (2019).
11. Bisagno, V. & Cadet, J. L. in *Handbook of Neurotoxicity* (ed. Kostrzewa, R.M.) 563–585 (Springer, 2022).
12. Grandy, D. K. in *Neuropathology of Drug Addictions and Substance Misuse* (ed. Preedy, V. R.) 108–116 (Academic Press, 2016).
13. Miller, G. M. The emerging role of trace amine-associated receptor 1 in the functional regulation of monoamine transporters and dopaminergic activity. *J. Neurochem.* **116**, 164–176 (2011).
14. Berry, M. D. Mammalian central nervous system trace amines. Pharmacologic amphetamines, physiologic neuromodulators. *J. Neurochem.* **90**, 257–271 (2004).
15. Tonelli, M. & Cichero, E. Trace amine associated receptor 1 (TAAR1) modulators: a patent review (2010–present). *Expert Opin.Ther. Pat.* **30**, 137–145 (2020).
16. Xu, Z. & Li, Q. TAAR agonists. *Cell. Mol. Neurobiol.* **40**, 257–272 (2020).
17. Achat-Mendes, C., Lynch, J. J., Sullivan, K. A., Vallender, E. J. & Miller, G. M. Augmentation of methamphetamine-induced behaviors in transgenic mice lacking the trace amine-associated receptor 1. *Pharmacol. Biochem. Behav.* **101**, 201–207 (2012).
18. Cotter, R. et al. The trace amine-associated receptor 1 modulates methamphetamine's neurochemical and behavioral effects. *Front. Neurosci.* **9**, 39 (2015).
19. Underhill, S. M. et al. Amphetamines signal through intracellular TAAR1 receptors coupled to Go13 and GoS in discrete subcellular domains. *Mol. Psychiatry* **26**, 1208–1223 (2021).
20. Eyun, S.-i., Moriyama, H., Hoffmann, F. G. & Moriyama, E. N. Molecular evolution and functional divergence of trace amine-associated receptors. *PLoS ONE* **11**, e0151023 (2016).
21. Accoroni, A. & Zucchi, R. in *Trace Amines and Neurological Disorders* (eds Farooqui, T. & Farooqui, A. A.) 151–164 (Academic Press, 2016).
22. Liberles, S. D. Trace amine-associated receptors: ligands, neural circuits, and behaviors. *Curr. Opin. Neurobiol.* **34**, 1–7 (2015).
23. Alnfees, Y. et al. Trace amine-associated receptor 1 (TAAR1): potential application in mood disorders: a systematic review. *Neurosci. Biobehav. Rev.* **131**, 192–210 (2021).
24. Lothar, L. et al. Trace amine-associated receptor 1 modulates dopaminergic activity. *J. Pharmacol. Exp. Ther.* **324**, 948 (2008).
25. Revel, F. G. et al. A new perspective for schizophrenia: TAAR1 agonists reveal antipsychotic- and antidepressant-like activity, improve cognition and control body weight. *Mol. Psychiatry* **18**, 543–556 (2013).
26. Wu, R. & Li, J.-X. Potential of ligands for trace amine-associated receptor 1 (TAAR1) in the management of substance use disorders. *CNS Drugs* **35**, 1239–1248 (2021).
27. Galley, G., Stalder, H., Goergler, A., Hoener, M. C. & Norcross, R. D. Optimisation of imidazole compounds as selective TAAR1 agonists: discovery of RO5073012. *Bioorg. Med. Chem. Lett.* **22**, 5244–5248 (2012).
28. Galley, G. et al. Discovery and characterization of 2-aminooxazolines as highly potent, selective, and orally active TAAR1 agonists. *ACS Med. Chem. Lett.* **7**, 192–197 (2016).
29. Raony, I., Dornith, I., Lourenco, M. V., Paes-de-Carvalho, R. & Pandolfo, P. Trace amine-associated receptor 1 modulates motor hyperactivity, cognition, and anxiety-like behavior in an animal model of ADHD. *Prog. Neuropsychopharmacol. Biol. Psychiatry* **117**, 110555 (2022).
30. Pei, Y. et al. Activation of the trace amine-associated receptor 1 prevents relapse to cocaine seeking. *Neuropsychopharmacology* **39**, 2299–2308 (2014).
31. Barak, L. S. et al. Pharmacological characterization of membrane-expressed human trace amine-associated receptor 1 (TAAR1) by a bioluminescence resonance energy transfer cAMP biosensor. *Mol. Pharmacol.* **74**, 585–594 (2008).
32. Saarinen, M. et al. TAAR1 dependent and independent actions of the potential antipsychotic and dual TAAR1/5-HT1A receptor agonist SEP-383856. *Neuropsychopharmacology* **47**, 2319–2329 (2022).
33. Xu, P. et al. Structural insights into the lipid and ligand regulation of serotonin receptors. *Nature* **592**, 469–473 (2021).
34. Reese, E. A., Bunzow, J. R., Arttamangkul, S., Sonders, M. S. & Grandy, D. K. Trace amine-associated receptor 1 displays species-dependent stereoselectivity for isomers of methamphetamine, amphetamine, and para-hydroxyamphetamine. *J. Pharmacol. Exp. Ther.* **321**, 178–186 (2007).
35. Chun, E. et al. Fusion partner toolchest for the stabilization and crystallization of G protein-coupled receptors. *Structure* **20**, 967–976 (2012).
36. Duan, J. et al. Cryo-EM structure of an activated VIP1 receptor-G protein complex revealed by a NanoBiT tethering strategy. *Nat. Commun.* **11**, 4121 (2020).
37. Liu, P. et al. The structural basis of the dominant negative phenotype of the Gαi1β1γ2 G203A/A326S heterotrimer. *Acta Pharmacol. Sin.* **37**, 1259–1272 (2016).
38. Maeda, S. et al. Development of an antibody fragment that stabilizes GPCR/G-protein complexes. *Nat. Commun.* **9**, 3712 (2018).
39. Isberg, V. et al. Generic GPCR residue numbers - aligning topology maps while minding the gaps. *Trends Pharmacol. Sci.* **36**, 22–31 (2015).
40. Zhuang, Y. et al. Structural insights into the human D1 and D2 dopamine receptor signaling complexes. *Cell* **184**, 931–942.e918 (2021).
41. Tan, E. S. et al. The molecular basis of species-specific ligand activation of trace amine-associated receptor 1 (TAAR1). *ACS Chem. Biol.* **4**, 209–220 (2009).
42. Cichero, E., Espinoza, S., Gainetdinov, R. R., Brasili, L. & Fossa, P. Insights into the structure and pharmacology of the human trace amine-associated receptor 1 (hTAAR1): homology modelling and docking studies. *Chem. Biol. Drug Des.* **81**, 509–516 (2013).
43. Liao, S., Pino, M. J. Jr., Deleon, C., Lindner-Jackson, M. & Wu, C. Interaction analyses of hTAAR1 and mTAAR1 with antagonist EPPTB. *Life Sci.* **300**, 120553 (2022).
44. Reese, E. A. et al. Exploring the determinants of trace amine-associated receptor 1's functional selectivity for the stereoisomers of amphetamine and methamphetamine. *J. Med. Chem.* **57**, 378–390 (2014).
45. Huang, S. et al. GPCRs steer G(i) and G(s) selectivity via TM5-TM6 switches as revealed by structures of serotonin receptors. *Mol. Cell* **82**, 2681–2695.e2686 (2022).
46. Su, M. et al. Structures of β1-adrenergic receptor in complex with G_s and ligands of different efficacies. *Nat. Commun.* **13**, 4095 (2022).
47. Kaplan, A. L. et al. Bespoke library docking for 5-HT2A receptor agonists with antidepressant activity. *Nature* **610**, 582–591 (2022).
48. Tan, Y. et al. Structural insights into the ligand binding and G_i coupling of serotonin receptor 5-HT5A. *Cell Discov.* **8**, 50 (2022).
49. Borowsky, B. et al. Trace amines: Identification of a family of mammalian G protein-coupled receptors. *Proc. Natl. Acad. Sci. USA* **98**, 8966–8971 (2001).
50. Zhang, Y. et al. Single-particle cryo-EM structural studies of the β2AR-G_s complex bound with a full agonist formoterol. *Cell Discov.* **6**, 45 (2020).
51. Imai, S. et al. Structural equilibrium underlying ligand-dependent activation of β2-adrenoreceptor. *Nat. Chem. Biol.* **16**, 430–439 (2020).
52. Staus, D. P. et al. Allosteric nanobodies reveal the dynamic range and diverse mechanisms of G-protein-coupled receptor activation. *Nature* **535**, 448–452 (2016).
53. Lam, V. M. et al. Behavioral effects of a potential novel TAAR1 antagonist. *Front. Pharmacol.* **9**, 953 (2018).
54. Bradai, A. et al. The selective antagonist EPPTB reveals TAAR1-mediated regulatory mechanisms in dopaminergic neurons of the mesolimbic system. *Proc. Natl. Acad. Sci. USA* **106**, 20081–20086 (2009).
55. Guo, L. et al. Structural basis of amine odorant perception by a mammal olfactory receptor. *Nature* **618**, 193–200 (2023).

Publisher's note Springer Nature remains neutral with regard to jurisdictional claims in published maps and institutional affiliations.

Springer Nature or its licensor (e.g. a society or other partner) holds exclusive rights to this article under a publishing agreement with the author(s) or other rightsholder(s); author self-archiving of the accepted manuscript version of this article is solely governed by the terms of such publishing agreement and applicable law.

© The Author(s), under exclusive licence to Springer Nature Limited 2023

Methods

Cell lines

Spodoptera frugiperda (Sf9, Expression systems) and *Trichoplusia ni*. (High Five, Thermo Fisher) cells were grown in ESF 921 medium at 27 °C and 120 rpm. HEK293T cells were grown in a humidified 37 °C incubator with 5% CO₂ using media supplemented with 100 IU ml⁻¹ penicillin and 100 mg ml⁻¹ streptomycin (Invitrogen). The human cell lines HEK293T were maintained in Dulbecco's Modified Eagle Medium (VWR) containing 10% fetal bovine serum (FBS, VWR).

Constructs

For structure determination of the METH and SEP-363856 activated TAAR1-G_s complex, the full-length gene sequence of wild-type human TAAR1 was cloned into pFastBac vector with an N-terminal haemagglutinin-signalling peptide sequence followed by a Flag tag, a 10X His tag and a thermostabilized *Escherichia coli* apocytochrome *b*562RIL (BRIL) to facilitate expression and purification³⁵. The NanoBiT tethering method was used to facilitate assembly of the TAAR1 complexes, in which the C terminus of TAAR1 was fused to the large part of NanoBiT (LgBiT), and the C terminus of Gβ was fused to the small part of NanoBiT (SmBiT)³⁶. A dominant-negative form of human Gα_s (DN_Gα_s) was constructed by site-directed mutagenesis to incorporate mutations G226A and A366S to decrease the affinity of nucleotide binding to the heterotrimer Gαβγ complex³⁷. To obtain a well-performed METH-TAAR1-G_s complex sample, a miniGα_s format including mutations G226A and A366S (DN_miniGα_s) was constructed by removing the α-helical domain of Gα_s and introducing mutations according to the previously reported miniGα_s sequence^{56,57}. All the three G-protein complex components, DN_Gα_s/DN_miniGα_s, rat Gβ₁ and bovine Gγ₂, were cloned into pFastBac vector separately.

For structure determination of the RO5256390 and β-PEA-activated TAAR1-G_s complex, the wild-type human TAAR1 construct was cloned into the pFastBac1 vector with the N-terminal haemagglutinin-signalling peptide followed by a Flag tag, 10X His tag and human rhinovirus 3C protease site. To enhance surface expression of the receptor, a BRIL fusion protein was fused at the N terminus of TAAR1 linked by the first nine amino acids of the β₂-adrenergic receptor (MGQPGNGSA, β9)³¹. An engineered miniGα_s was fused to the C terminus of TAAR1 with three copies of 3C protease sites between them. Gβ₁ and Gγ₂ were cloned into a pFastBac Dual vector.

For structure determination of SEP-363856 activated 5-HT_{1A}R-G_i complex, the constructs are followed as indicated in previous work³³. In short, the human 5-HT_{1A}R with thermally stabilized mutation L125^{3,41}W, 24 residues truncated at the N terminus, N-terminal Flag tag and His tag followed by a BRIL fusion protein were cloned into the pFastBac vector. A dominant-negative human Gα_{ii} was generated by site-directed mutagenesis to incorporate mutations S47N, G203A, A326S and E245A, which improve the dominant-negative effect by weakening a salt bridge that helps to stabilize the interactions with the βγ subunits³⁷. Human dominant-negative_Gα_{ii}, human Gβ₁, human Gγ₂ and a single-chain antibody scFv16 were cloned into pFastBac vectors separately.

Expression, complex formation and purification

The complexes are all expressed in Hi5 insect cells (Invitrogen). For expression of METH- or SEP-363856-activated TAAR1-G_s complex, cell cultures were grown in ESF 921 medium (Expression system) to a density of 3 × 10⁶ ml⁻¹ with virus preparations for TAAR1, DN_Gα_s/DN_miniGα_s, Gβ₁ and Gγ₂, at the ratio of 1:1:1:1. For expression of SEP-363856-activated 5-HT_{1A}R-G_i complex, virus preparations for 5-HT_{1A}R, scFv16, DN_Gα_{ii}, Gβ₁ and Gγ₂, at the ratio of 1:1:1:1 were added. For expression of β-PEA or RO5256390-activated TAAR1-G_s complex, cell cultures were grown in ESF 921 medium to a density of 3 × 10⁶ ml⁻¹ with two separate virus preparations for TAAR1-miniGα_s and Gβ₁γ₂ at a ratio of 1:1.2. The infected

cells were cultured at 27 °C for 48 h before collection by centrifugation and the cell pellets were stored at -80 °C for future use.

For the purification of the four TAAR1-G_s complexes, cell pellets from 1 litre of culture were thawed at room temperature and re-suspended in low-salt buffer containing 20 mmol HEPES pH 7.4, 100 mmol NaCl, 5 mmol CaCl₂, 5 mmol MgCl₂, 10% glycerol, protease inhibitor cocktail (Thermo Fisher). The TAAR1-G_s complexes were formed on a membrane in the presence of 600 μmol METH or 200 μmol SEP-363856 (Target-mol, US) or 10 μmol RO5256390 (Sigma) or 200 μmol β-PEA (Tocris) and treated with apyrase (20 mU ml⁻¹, NEB), followed by incubation overnight at 4 °C. Cell membranes were collected by ultra-centrifugation at 100,000×g for 40 min. The membranes were re-suspended and then incubated with 600 μmol METH or 200 μmol SEP-363856 or 5 μmol RO5256390 or 100 μmol β-PEA, 2 mg ml⁻¹ iodoacetamide (Sigma), 20 mU ml⁻¹ apyrase at 4 °C for 1 h. The protein was extracted from the membrane by 20 mmol HEPES, pH 7.4, 100 mmol NaCl, 5 mmol CaCl₂, 5 mmol MgCl₂, 10% glycerol, 1% (w/v) lauryl maltose neopentyl glycol (LMNG, Anatrace), 0.2% (w/v) cholestryl hemisuccinate Tris salt (CHS, Anatrace) and stirred for 2.5 h at 4 °C. The supernatant was isolated by centrifugation at 30,000 r.p.m. for 30 min and then incubated overnight at 4 °C with pre-equilibrated TALON IMAC resin (Clontech). After batch binding, the TALON IMAC resin with immobilized protein complex was manually loaded onto a gravity flow column. The TALON IMAC resin was washed with 10 column volumes of 20 mmol HEPES, pH 7.4, 100 mmol NaCl, 5 mmol CaCl₂, 5 mmol MgCl₂, 30 mmol imidazole, 10% glycerol, 0.1% LMNG (w/v), 0.02% CHS (w/v), 200 μmol METH or 100 μmol SEP-363856 or 10 μmol RO5256390 or 200 μmol β-PEA and eluted with the same buffer plus 300 mmol imidazole, 600 μmol METH or 200 μmol SEP-363856 or 20 μmol RO5256390 or 400 μmol β-PEA. The eluted protein was incubated with 20 μg ml⁻¹ of Nb35 at 4 °C for another 2 h. The mixture was then purified by SEC using a Superdex 200 10/300 GL column (GE healthcare) or Superose 6 10/300 GL column (GE healthcare) in 20 mmol HEPES, pH 7.4, 100 mmol NaCl, 0.00075% (w/v) LMNG, 0.00025% (w/v) CHS and 200 μmol METH or 100 μmol SEP-363856 or 1 μmol RO5256390 or 40 μmol β-PEA. The fractions of monomeric complex were collected and concentrated to 2.9–4.0 mg ml⁻¹ for electron microscopy experiments. For structure determination of the SEP-363856-activated 5-HT_{1A}R-G_i complex, the purification followed the same protocol as that of the SEP-363856-activated TAAR1-G_s complex mentioned above.

Cryo-EM grid preparation and data collection

For cryo-EM grid preparation, samples for the METH- or SEP-363856- or RO5256390- or β-PEA-bound TAAR1-G_s complex at a concentration of 2.9–4.0 mg ml⁻¹, and SEP-363856-activated 5-HT_{1A}R-G_i complex at a concentration of 5 mg ml⁻¹, were applied individually to electron microscopy grids (Quantifoil, 300 mesh Au R1.2/1.3) that were glow discharged for 45 s, blotted for 4 s under 100% humidity at 4 °C before being plunged into liquid ethane cooled by liquid nitrogen using a Mark IV Vitrobot (FEI). Protein concentration was determined by absorbance at 280 nm using a Nanodrop 2000 Spectrophotometer (Thermo Fisher Scientific).

For METH-bound TAAR1-G_s complex, cryo-EM imaging was collected on a Titan Krios equipped with a Falcon 4 direct electron detection device at 300 kV at the Shanghai Advanced Electron Microscope Center, Shanghai Institute of Material Medica. Images were taken with a pixel size of 0.73 Å, a defocus ranging from -1.0 to -2.0 μm using the EPU software (FEI Eindhoven, Netherlands). Each micrograph was dose-fractionated to 36 frames with a total dose of 50 e⁻ Å⁻² on each electron event representation (EER) format video. For SEP-363856-bound TAAR1-G_s or 5-HT_{1A}R-G_i complex, cryo-EM data were collected at the Shanghai Advanced Electron Microscope Center, Shanghai Institute of Material Medica, performed on a Titan Krios at a 300 kV accelerating voltage, using a K3 Summit direct electron detector (Gatan) with a Gatan energy filter (operated with a slit width of 20 eV) in counting

mode at a calibrated magnification of 0.824 Å per pixel. Micrographs were obtained at a dose rate of about $8.0 \text{ e}^- \text{ Å}^{-2} \text{ s}^{-1}$ with a defocus ranging from -1.0 to $-2.0 \mu\text{m}$. Each micrograph was dose-fractionated to 36 frames with a total dose of $50 \text{ e}^- \text{ Å}^{-2}$. For the RO5256390- or β -PEA-bound TAARI-G_s complex, cryo-EM data were collected at the Bio-EM platform of ShanghaiTech University, performed on a Titan Krios at a 300 kV accelerating voltage, using a K3 Summit direct electron detector (Gatan) with a Gatan energy filter (operated with a slit width of 20 eV) in counting mode at a calibrated magnification of 0.832 Å per pixel and a defocus range of -1 to $-2 \mu\text{m}$. Each video comprised 40 frames with a total dose of $60 \text{ e}^- \text{ Å}^{-2}$, exposure time was 2.0 s with the dose rate of $20 \text{ e}^- \text{ per pixel s}^{-1}$ using serial electron microscopy⁵⁸.

Image processing

All dose-fractionated images were motion-corrected and dose-weighted by MotionCorr2⁵⁹ software, and their contrast transfer functions (CTF) were estimated by patch CTF estimation in cryoSPARC v.3.2.0 (ref. 60). For the METH-TAARI-G_s complex, auto-picking by blob picker produced particles that were subjected to two-dimensional (2D) and three-dimensional (3D) classifications. Representative classes were picked as templates for template-picking. The template-picking process produced 6,088,230 particles which were subjected to interactive 2D and 3D classifications, producing 928,277 particles with complete complex and good quality. The selected particles were further subjected to several rounds of ab-initial reconstruction and heterogeneous refinement, resulting in a well-defined subset with 483,727 particles. Subsequent heterogeneous refinement, non-uniform refinement and local refinement generated a map with an indicated global resolution of 2.8 Å reconstructed by 306,504 particles.

For the SEP-383656-TAARI-G_s complex, auto-picking by blob picker produced particles that were subjected to 2D and 3D classifications. Representative classes were picked as templates for template-picking. The template-picking process produced 6,138,879 particles which were subjected to interactive 2D and 3D classifications, producing 2,243,894 particles with complete complex and good quality. The selected particles were further subjected to several rounds of ab-initial reconstruction and heterogeneous refinement, resulting in a well-defined subset with 824,418 particles. Subsequent heterogeneous refinement, non-uniform refinement and local refinement generated a map with an indicated global resolution of 2.6 Å by reconstruction of 664,918 particles.

For the RO5256390-TAARI-G_s complex, 300 images were selected automatically to do blob picking, and 154,707 particles were picked and extracted, then 2D classification with 200 classes to sort the dataset was performed in cryoSPARC v.3.2.0 and 15 classes with 26,599 particles were selected as training data to generate a deep-learning model using topaz. The deep picker was performed on all 5,135 images using topaz with the pretrained model, and a total of 2,305,822 particles were auto-picked and used in 2D classification. A total of 1,644,726 particle projections were then selected for the subsequent 3D heterogeneous refinement in cryoSPARC. After the final round of 3D heterogeneous refinement from 268,242 particle projections, a selected subset containing 145,907 projections that displayed fine structural details were processed for high-resolution refinement, including non-uniform refinement and local refinement, resulting in the final map with an overall resolution of 2.8 Å.

For the β -PEA-TAARI-G_s complex, data processing was performed following similar procedures. From 4,371 micrographs, a total of 1,980,963 particles were extracted using topaz for further 2D classification, and four different conformational subclasses were obtained by 3D heterogeneous refinement. Finally, 87,235 particles of the best class were used for non-uniform refinement and local refinement in cryoSPARC and the best-density map was obtained with a nominal resolution of 3.0 Å.

For the SEP-363856-5-HT_{1A}R-G_i complex, particle selection and 2D, 3D classifications were performed using cryoSPARC. Blob picking

of 100 images produced 87,185 particles that were subjected to 2D classification. Representative classes were picked as templates for auto-picking. The auto-picking process produced 5,708,684 particles, which were subjected to interactive 2D and 3D classifications, producing 970,684 particles with complete complex and good quality. The selected particles were further subjected to several rounds of ab-initial reconstruction and heterogeneous refinement, resulting in a well-defined subset with 396,934 particles. Subsequent non-uniform refinement and local refinement generated a map with an indicated global resolution of 3.0 Å. The overall resolution was estimated on the basis of gold-standard Fourier shell correlation of independently refined half maps and the 0.143 cutoff criterion. Local resolution was estimated in cryoSPARC using default parameters.

Model building, refinement, and validation

For the four TAAR-G_s complexes, the active state of TAARI from AlphaFold prediction⁶¹ is used as the starting model for model building; the D1R-G_s complex structure⁴⁰ (PDB: 7JVQ) was used as starting models for model building and refinement against the electron density map of G proteins and Nb35. For the SEP-363856-5-HT_{1A}R-G_i complex, the 5-HT_{1A}R-G_i-complex structure³³ (PDB: 7e2y) was used as starting models for model building and refinement against the electron density map. The cryo-EM model was docked into the electron microscopy density map using Chimera-1.14 (ref. 62), followed by iterative manual adjustment and rebuilding in COOT-0.9.6 (ref. 63) and ISOLDE-1.2 (ref. 64). Restraints for METH, SEP-383656, RO5256390 and β -PEA were generated using Phenix.elbow⁶⁵ from SMILES string inputs and optimized with the eLBOW AM1 QM method in PHENIX Real space, and reciprocal space refinements were performed using Phenix programmes with secondary structure and geometry restraints. The final refinement statistics are provided in Extended Data Table 1. UCSF Chimera-1.14 (ref. 62), Chimera X⁶⁶, and PyMOL-2.0 (<https://pymol.org/2/>) were used to prepare the structural figures in the paper.

GloSensor cAMP assay

The GloSensor cAMP assay (Promega)⁶⁷ was performed to monitor the real-time cAMP variation induced by TAARI or 5-HT_{1A}R. In brief, the full-length TAARI/5-HT_{1A}R were fused after haemagglutinin signalling peptide and Flag tag. The constructs were cloned into the pcDNA3.0 vector for the HEK293T system. Before transfection, HEK293T cells were plated onto six-well plates with a density of 2×10^5 cells ml⁻¹. After 16 h, cells were transfected with 1.5 µg receptor and 1.0 µg GloSensor-22F (Promega). After 24 h, transfected cells were digested and transferred onto 96-well plate with 50 µl suspension with density of 3×10^5 cells ml⁻¹. After another 16 h, cells were starved by 50 µl Hank's balanced salt solution for 30 min and then incubated in 50 µl CO₂-independent media containing 2% GloSensor cAMP Reagent (Promega) for 1 h. After incubation, 5.5 µl test ligands with various concentrations were added and incubated for 10 min at room temperature. For G_i-coupled 5-HT_{1A}R, additional 5.5 µl Forskolin were added to the cells in the final concentration of 1 µmol. All luminescence signals were tested by an EnVision multi-plate reader according to the manufacturer's instructions. All data were analysed using Prism 9 (GraphPad) and presented as means \pm s.e.m. from at least three independent experiments in technical duplicates or triplicates. Non-linear curve fit was performed using a three-parameter logistic equation (log (agonist versus response)). The final curves were shown as normalization form compared with the wild type. The significance was determined with two-side, one-way analysis of variance followed by Fisher's LSD test compared with WT. *P < 0.05; **P < 0.01 and ***P < 0.001 were considered as statistically significant.

G_s recruitment assay

The NanoBiT Protein-Protein interaction system (Promega) was performed to measure G_s protein recruitment of TAARI. In brief, HEK293 cells were cotransfected with plasmids encoding TAARI-LgBiT and

Article

SmBiT-miniGαs at the ratio of 1:1.5. After 24 h, transfected cells were harvested and re-suspended in PBS buffer. The cells were diluted to a density of 600,000 cells ml⁻¹. Then 10 µl cell suspension was transferred into a 384-well plate and loaded with 10 µl compounds (3X). This was briefly centrifuged, 10 µl coelenterazine 400a (Yeasen) was added, with a final concentration of 50 µmol. After being incubated for 10 min at room temperature, luminescence was measured with an EnVision multi-plate reader (PerkinElmer).

Radioligand-binding assay

Binding assays for TAAR1 were performed using Hi5 insect cell membranes expressing the TAAR1 construct. Cell pellets from 50 ml culture were re-suspended in low-salt buffer containing 20 mmol HEPES pH 7.4, 100 mmol NaCl, 5 mmol CaCl₂, 5 mmol MgCl₂, 10% glycerol protease inhibitors. The assays were conducted in a 96-well plate in the standard binding buffer (50 mmol HEPES, 5 mmol MgCl₂, 0.5 mmol EDTA, pH 7.4) using [³H]-RO5192022 (TAARI)⁶⁸.

For displacement experiments, increasing concentrations of compounds were incubated with membrane and radioligands 1–3 nmol for 2 h at room temperature in the dark. The reaction was terminated by rapid vacuum filtration onto chilled 0.3% polyethyleneimine (PEI)-soaked glass fibre/A (GF/A) filters followed by three quick washes with cold washing buffer (50 mM Tris-HCl, pH 7.4). Counts per minute (CPM) was counted on MicroBeta TriLux reader (PerkinElmer). Data were analysed with GraphPad Prism 8.0 using ‘One-site-Fit K_i’ to yield K_i.

Saturation binding assays with 0–80 nmol [³H]-RO5192022 in TAAR1 standard binding buffer were performed to determine equilibrium dissociation constants (K_d), whereas 10 µmol β-PEA was used to define nonspecific binding. The reaction was incubated in the dark for 2 h and terminated by rapid vacuum filtration as described above. Data were analysed with GraphPad Prism 8.0 using ‘One-site-specific binding’ to yield K_d.

α,β-dissociation assay

Chimeric constructs were designed and assays were performed as previously described (BRET assay)⁶⁹. HEK293T (ATCC CRL-11268; mycoplasma free) were plated either in 6-cm dishes at a density of 1–2 million cells per well. Next, cells were transfected at a confluence of 60–80% at 12–14 h later, using a 1:1:1:1 DNA ratio of 5-HT_{1A}R:Gαi1-RLuc8:Gβ3:Gγ9-GFP2 (1 µg per construct for 6-cm dishes). Polyethyleneimine was used to complex the DNA at a ratio of 4 µl per µg DNA. After 24 h, cells were re-seeded in white opaque bottom 96-well assay plates (Beyotime) at a density of 30,000–50,000 cells per well. One day after plating in 96-well assay plates, the growth medium was carefully decanted and replaced immediately with 40 µl drug buffer (one Hank’s balanced salt solution and 20 mmol HEPES, pH 7.4) containing 7.5 µmol coelenterazine 400a (Goldbio). After a 2-min equilibration period, cells were treated with 20 µl compounds prepared in drug buffer at a serial concentration gradient for an additional 5 min. Plates were then read in an LB940 Mithras plate reader (Berthold Technologies) with 395 nm (RLuc8-coelenterazine 400a) and 510 nm (GFP2) emission filters, at integration times of 1 s per well. BRET ratios were computed as the ratio of the GFP2 emission to RLuc8 emission.

Surface-expression analysis

For GloSensor assay, cell-surface expression for wild type and mutants of TAAR1 was monitored by a fluorescence-activated cell sorting (FACS) assay in a high-throughput mode. Briefly, the anti-Flag fluorescein isothiocyanate (FITC) (2.5 µg ml⁻¹) was added to cells to quantify the percentage of cells with surface-expressing TAAR1 and the density (mean fluorescence intensity) of TAAR1 on the surface of those cells. anti-Flag FITC (2.5 µg ml⁻¹) with 1.5% Triton was added to cells to quantify the total expression levels which includes total percentage and total density. For total and surface FITC expression assay, we used 10 µl FITC with and without Triton working solution plus 10 µl of cells incubated at 4 °C for

20 min, added 180 µl of one TBS (tris-buffered saline) (straight TBS, without bovine serum albumin (BSA)), then ran the assay on a Guava flow cytometer. The surface and total expression data are summarized in Supplementary Table 6.

For 5-HT_{1A}R, the surface expression was also monitored by FACS assay. In brief, HEK293 cells expressing Flag-tagged 5-HT_{1A}R were harvested at 24 h posttransfection and suspended by PBS buffer with 5 mmol EDTA and blocked with 5% (w/v) BSA at room temperature for 15 min, then followed by the incubation with 200 µl of 1:300 anti-Flag M2 antibody (Sigma, catalogue no. F3165) at room temperature for 1 h. Cells were washed with 1% (w/v) BSA in PBS three times and incubated with 200 µl 1:1000 anti-mouse Alexa Fluor 488 conjugated secondary antibody (Invitrogen, catalogue no. A11029) at 4 °C in the dark. After three times washing as above, cells were re-suspended in 200 µl 1% (w/v) BSA in PBS for detection by Accuri C6 flow cytometer (BD biosciences). The final expression data are summarized and integrated in Supplementary Table 5.

Modelling and molecular docking

The homology modelling of rat and mouse TAAR1 structures were conducted based on the METH-hTAAR1 complex structure using MODELLER⁷⁰. The sequence of the hTAAR1 in our cryo-EM structure served as the reference. Following sequence alignment, the AutoModel function of MODELLER was employed for homology modelling. The structure boasting the lowest Discrete Optimized Protein Energy potential was selected for subsequent modelling stages.

The homology models of mouse and rat TAAR1 were subjected to docking procedures. These receptors were prepared using Schrödinger’s protein preparation wizard in Maestro. Initial steps included assigning bond orders and adding hydrogens to the protein. Concurrently, disulfide bonds were established, and residue heteroatom states were defined using Epik at a pH range of 7.0 ± 2.0. Subsequently, PROPKA3 was employed to designate residue protonation states. Grid files tailored for docking were generated based on the ligand-binding pocket. Ultimately, METH was docked to these grid files using the standard precision of the Glide programme. The pose exhibiting the best docking score was selected as the representative binding pose.

Molecular dynamic simulation analysis

The cryo-EM structures of human METH-TAAR1 and β-PEA-TAAR1 formed the foundation for their molecular dynamic simulations. Absent ICL3 structure was supplemented using the ICL3 modelled in the active state by AlphaFold multistate⁷¹. G proteins present in the complex were omitted. The rat and mouse models of METH-TAAR1 and β-PEA-TAAR1 had their ICL3 regions modelled using Modeller.

Protonation states for each residue were deduced using propka3 (ref. 72). Ligand parameterization was achieved with the CHARMM General Force Field⁷³. Subsequently, CHARMM-GUI was used to embed the models in a 70 × 70 Å POPC membrane⁷⁴, flanked by 15 Å of water on either side. A concentration of 0.15 mol NaCl, complemented with appropriate counterions, was introduced to each system via the distance method. Postassembly, the CHARMM36m force field was designated for amino acids and lipids⁷⁵.

Initially, the systems underwent a 5,000-cycle steepest descent minimization with constraints on backbone, sidechain, lipid coordinates and dihedrals. Gradual relaxation of constraints followed during the six-step equilibration process via CHARMM-GUI. Subsequently, production runs of three times 500 ns (for mouse or rat TAAR1) or six times 500 ns (for human TAAR1) were executed using pmemd.cuda in Amber20 (ref. 76). These runs, conducted in the isothermal-isobaric ensemble (NPT), maintained a temperature of 303.15 K and a pressure of 1 atm, regulated by the Nosé–Hoover thermostat and the Parrinello–Rahman barostat, respectively. Throughout these simulations, the Particle Mesh Ewald method catered to long-range electrostatic interactions. In contrast, short-range electrostatic and van der Waals interactions

were addressed with a 12 Å cutoff and gradually switched between 12 and 10 Å. The SHAKE algorithm was also invoked to restrain bonds with hydrogen, facilitating a 2 fs timestep.

Using the hieragllo algorithm, representative models were extracted from snapshots via the ‘cluster’ command in Amber’s CPPTRAJ. The binding free energy, including its decomposition to individual residues, was computed using the MM/GBSA method via the MMPBSA.py plugin in AmberTools20 (ref. 77).

Reporting summary

Further information on research design is available in the Nature Portfolio Reporting Summary linked to this article.

Data availability

Density maps and structure coordinates have been deposited in the Electron Microscopy Data Bank (EMDB) and the Protein Data Bank (PDB) with accession codes EMD-37347 and 8W87 for METH-TAAR1-G_s complex; EMD-37348 and 8W88 for SEP-363856-bound TAAR1-G_s complex; and EMD-37349 and 8W89 for β-PEA-bound TAAR1-G_s complex; EMD-37350 and 8W8A for RO5256390-TAAR1-G_s complex; and EMD-37351 and 8W8B for SEP-363856 bounded 5-HT_{1A}R-G_i protein complex. Source data are provided with this paper.

56. Carpenter, B., Nehmé, R., Warne, T., Leslie, A. G. & Tate, C. G. Structure of the adenosine A(2A) receptor bound to an engineered G protein. *Nature* **536**, 104–107 (2016).
57. García-Nafria, J., Lee, Y., Bai, X., Carpenter, B. & Tate, C. G. Cryo-EM structure of the adenosine A(2A) receptor coupled to an engineered heterotrimeric G protein. *eLife* **7**, e35946 (2018).
58. Mastronarde, D. N. Automated electron microscope tomography using robust prediction of specimen movements. *J. Struct. Biol.* **152**, 36–51 (2005).
59. Zheng, S. Q. et al. MotionCor2: anisotropic correction of beam-induced motion for improved cryo-electron microscopy. *Nat. Methods* **14**, 331–332 (2017).
60. Punjani, A., Rubinstein, J. L., Fleet, D. J. & Brubaker, M. A. cryoSPARC: algorithms for rapid unsupervised cryo-EM structure determination. *Nat. Methods* **14**, 290–296 (2017).
61. Jumper, J. et al. Highly accurate protein structure prediction with AlphaFold. *Nature* **596**, 583–589 (2021).
62. Pettersen, E. F. et al. UCSF Chimera—a visualization system for exploratory research and analysis. *J. Comput. Chem.* **25**, 1605–1612 (2004).
63. Emsley, P. & Cowtan, K. Coot: model-building tools for molecular graphics. *Acta Crystallogr. D* **60**, 2126–2132 (2004).
64. Croll, T. I. ISOLDE: a physically realistic environment for model building into low-resolution electron-density maps. *Acta Crystallogr. D* **74**, 519–530 (2018).
65. Adams, P. D. et al. Recent developments in the PHENIX software for automated crystallographic structure determination. *J. Synchrotron Radiat.* **11**, 53–55 (2004).
66. Pettersen, E. F. et al. UCSF ChimeraX: structure visualization for researchers, educators, and developers. *Protein Sci.* **30**, 70–82 (2021).
67. Wang, F. I., Ding, G., Ng, G. S., Dixon, S. J. & Chidiac, P. Luciferase-based GloSensor™ cAMP assay: temperature optimization and application to cell-based kinetic studies. *Methods* **203**, 249–258 (2022).
68. Revel, F. G. et al. Brain-specific overexpression of trace amine-associated receptor 1 alters monoaminergic neurotransmission and decreases sensitivity to amphetamine. *Neuropharmacology* **37**, 2580–2592 (2012).
69. Olsen, R. H. J. et al. TRUPATH, an open-source biosensor platform for interrogating the GPCR transducerome. *Nat. Chem. Biol.* **16**, 841–849 (2020).
70. Webb, B. & Sali, A. Comparative Protein Structure Modeling Using MODELLER. *Curr. Protoc. Bioinformatics* **54**, 5.6.1–5.6.37 (2016).
71. Heo, L. & Feig, M. Multi-state modeling of G-protein coupled receptors at experimental accuracy. *Proteins* **90**, 1873–1885 (2022).
72. Olsson, M. H., Søndergaard, C. R., Rostkowski, M. & Jensen, J. H. PROPKA3: consistent treatment of internal and surface residues in empirical pKa predictions. *J. Chem. Theory Comput.* **7**, 525–537 (2011).
73. Vanommeslaeghe, K. et al. CHARMM general force field: a force field for drug-like molecules compatible with the CHARMM all-atom additive biological force fields. *J. Comput. Chem.* **31**, 671–690 (2010).
74. Wu, E. L. et al. CHARMM-GUI Membrane Builder toward realistic biological membrane simulations. *J. Comput. Chem.* **35**, 1997–2004 (2014).
75. Huang, J. et al. CHARMM36m: an improved force field for folded and intrinsically disordered proteins. *Nat. Methods* **14**, 71–73 (2017).
76. Salomon-Ferrer, R., Götz, A. W., Poole, D., Le Grand, S. & Walker, R. C. Routine microsecond molecular dynamics simulations with AMBER on GPUs. 2. Explicit solvent particle mesh Ewald. *J. Chem. Theory Comput.* **9**, 3878–3888 (2013).
77. Miller, B. R. 3rd et al. MMPBSA.py: an efficient program for end-state free energy calculations. *J. Chem. Theory Comput.* **8**, 3314–3321 (2012).

Acknowledgements This work was partially supported by the Ministry of Science and Technology of China (2018YFA0507002 to H.E.X., 2020YFA0509102 to S.W.); the National Natural Science Foundation of China (32071194 to F.X., 32130022 and 82121005 to H.E.X., 52272087 to W.L., 82225025 and 32071197 to S.W.); Shanghai Municipal Science and Technology Major Project (2019SHZDZX02 to H.E.X.); CAS Strategic Priority Research Programme (XDB37030103 to H.E.X.); the Lingang Laboratory, grant no. LG-GG-202204-01 (H.E.X.); and the National Key R&D Program of China (2022YFC2703105 to H.E.X.). The cryo-EM data were collected at the Shanghai Advanced Electron Microscope Center, Shanghai Institute of Material Medica, as well as at the Bio-EM platform of ShanghaiTech University. We thank Q. Yuan, K. Wu, W. Hu and S. Zhang for providing technical support and assistance during data collection at the Shanghai Advanced Electron Microscope Center, Shanghai Institute of Material Medica; we thank Q. Sun, Z. Zhang, L. Wang, D. Liu and Y. Liu at the Bio-EM facility at ShanghaiTech University; and Q. Tan, Q. Shi, J. Liu, N. Chen, S. Hu and W. Xiao from ShanghaiTech University for protein cloning, expression, assay and data collection support. We thank S. Zhao from ShanghaiTech University, J. Wang from Institute of Biophysics, CAS, and Q. Li from Shanghai Jiaotong University to provide initial sets of TAAR1 tool compounds and suggestions for this work. We also thank the support from Shanghai Frontiers Science Center for Biomacromolecules and Precision Medicine at ShanghaiTech University.

Author contributions F.X. and H.E.X. initiated the project. H.L. designed and screened the expression constructs of TAAR1 and prepared protein samples of TAAR1-METH-G_s, TAAR1-SEP-363856-G_s, 5-HT_{1A}R-SEP-363856-G_s complexes for cryo-EM data collection, performed cryo-EM grids preparation, data acquisition, and structure determination, participated in GloSensor cAMP assay, and prepared the draft of the manuscript and figures. Y.Z. designed and screened the expression constructs of TAAR1 and prepared protein samples of TAAR1-β-PEA-G_s, TAAR1-RO5256390-G_s complexes for cryo-EM data collection, performed cryo-EM grids preparation, data acquisition and structure determination, and participated in manuscript editing and figure preparation. Y.W. performed GloSensor cAMP assay, G-protein recruitment assay and participated in figure preparation. Y.W. performed the radioligand-binding assay and Gαβ dissociation assay. X.-H. performed MD simulation analysis. P.X. and S.H. participated in protein sample preparation and structure determination. Q.Y. participated in data acquisition. X.Z. participated in G-protein recruitment assay. L.W. participated in GloSensor cAMP assay. K.J. assisted in some protein preparation work. H.C. assisted in compound preparation and synthesis. Z.L. helped construct the mutations for function assays. W.L. supervised compound preparation and synthesis. S.W. supervised ligand binding and functional assay. F.X. and H.E.X. conceived and supervised the project and participated in manuscript editing. F.X. and H.E.X. wrote the manuscript with input from H.L., Y.Z. and Y.W.

Competing interests The authors declare no competing interests.

Additional information

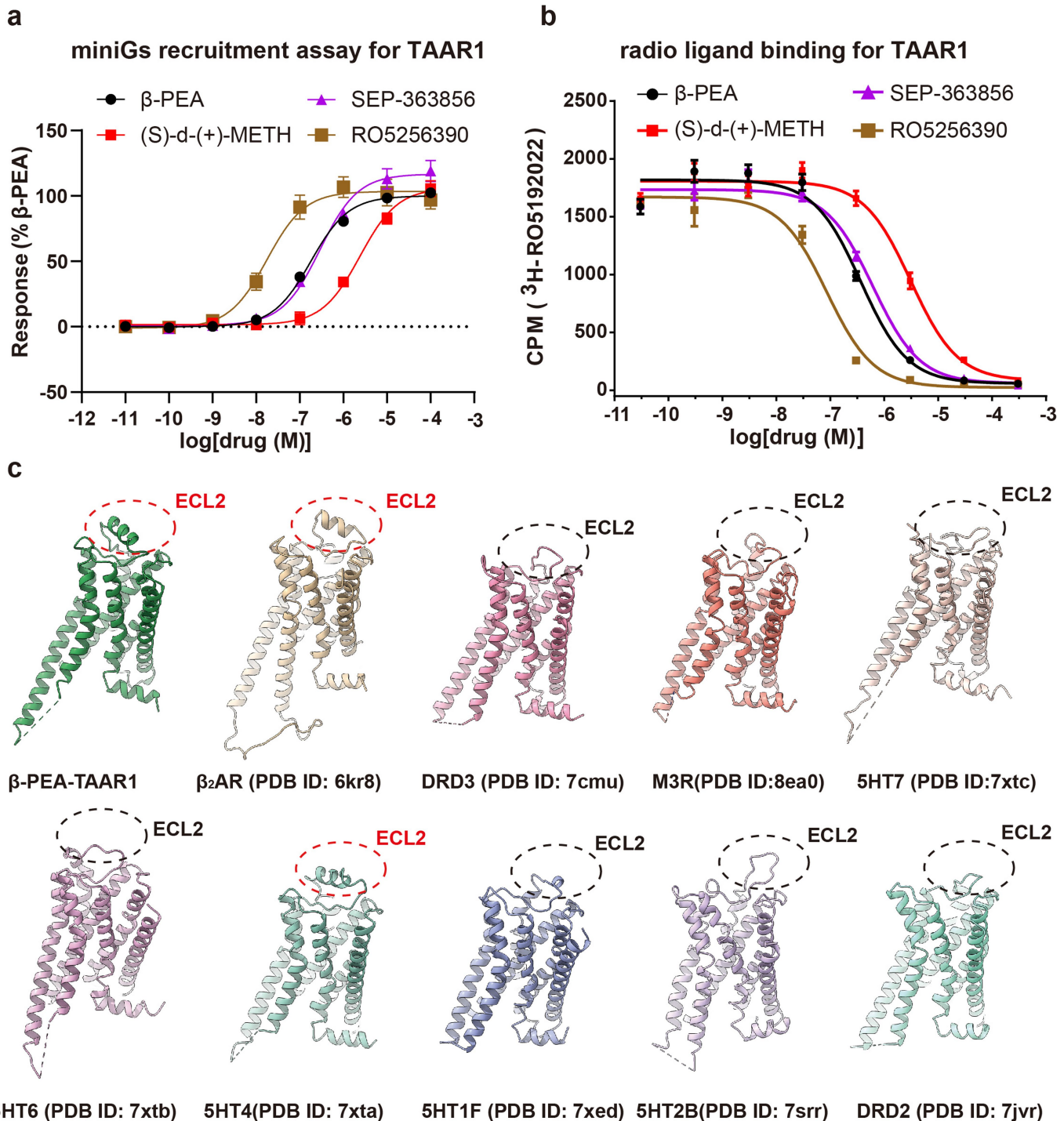
Supplementary information The online version contains supplementary material available at <https://doi.org/10.1038/s41586-023-06775-1>.

Correspondence and requests for materials should be addressed to Wenbin Liu, Sheng Wang, H. Eric Xu or Fei Xu.

Peer review information *Nature* thanks Thomas Keck, Tao Che and Harald Sitte for their contribution to the peer review of this work. Peer reviewer reports are available.

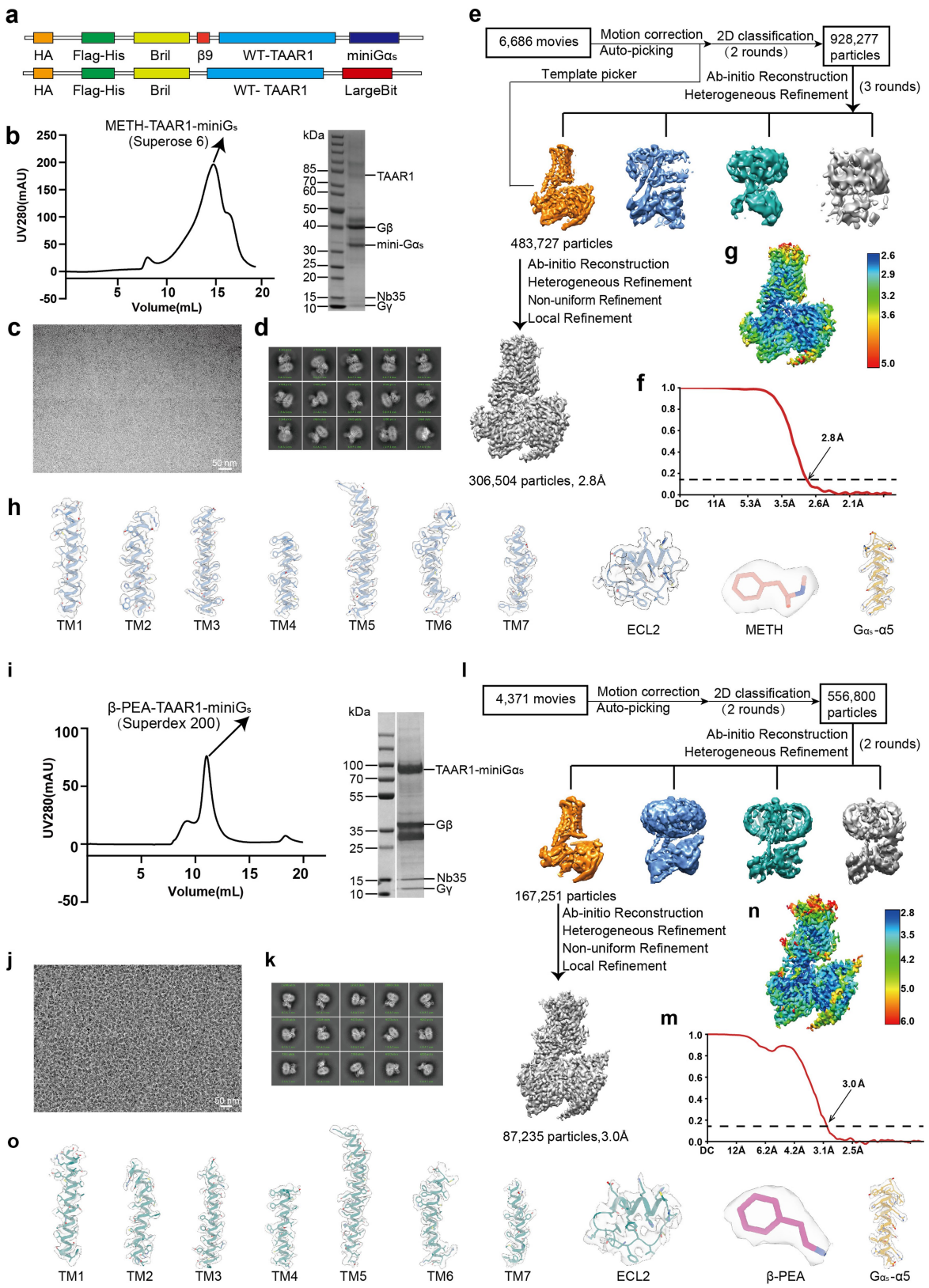
Reprints and permissions information is available at <http://www.nature.com/reprints>.

Article



Extended Data Fig. 1 | Functional assessment of TAAR1 by four agonists and structural feature of aminergic receptors. (a-b) Concentration–response curves of the four agonists activating TAAR1 evaluated by miniGs recruitment assay (a) and radio-ligand-binding assay (b). Data are mean \pm S.E.M. from 3

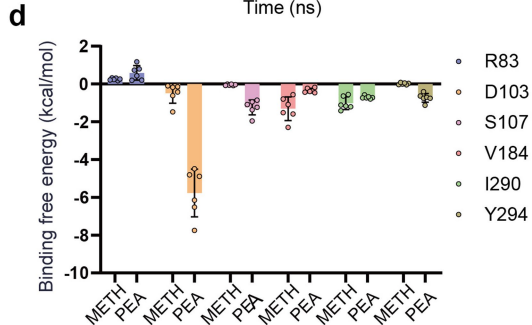
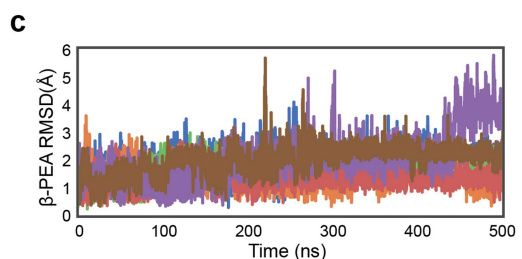
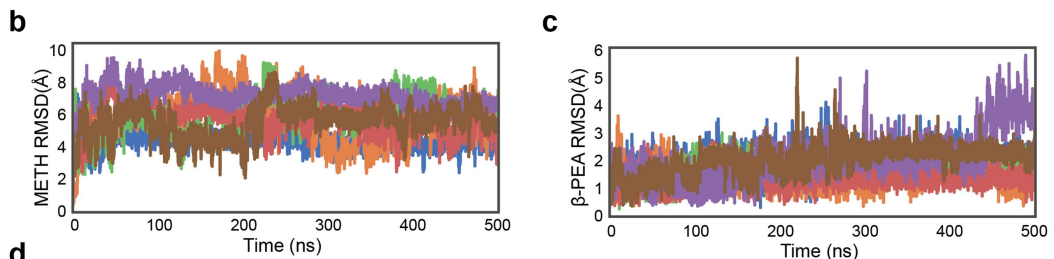
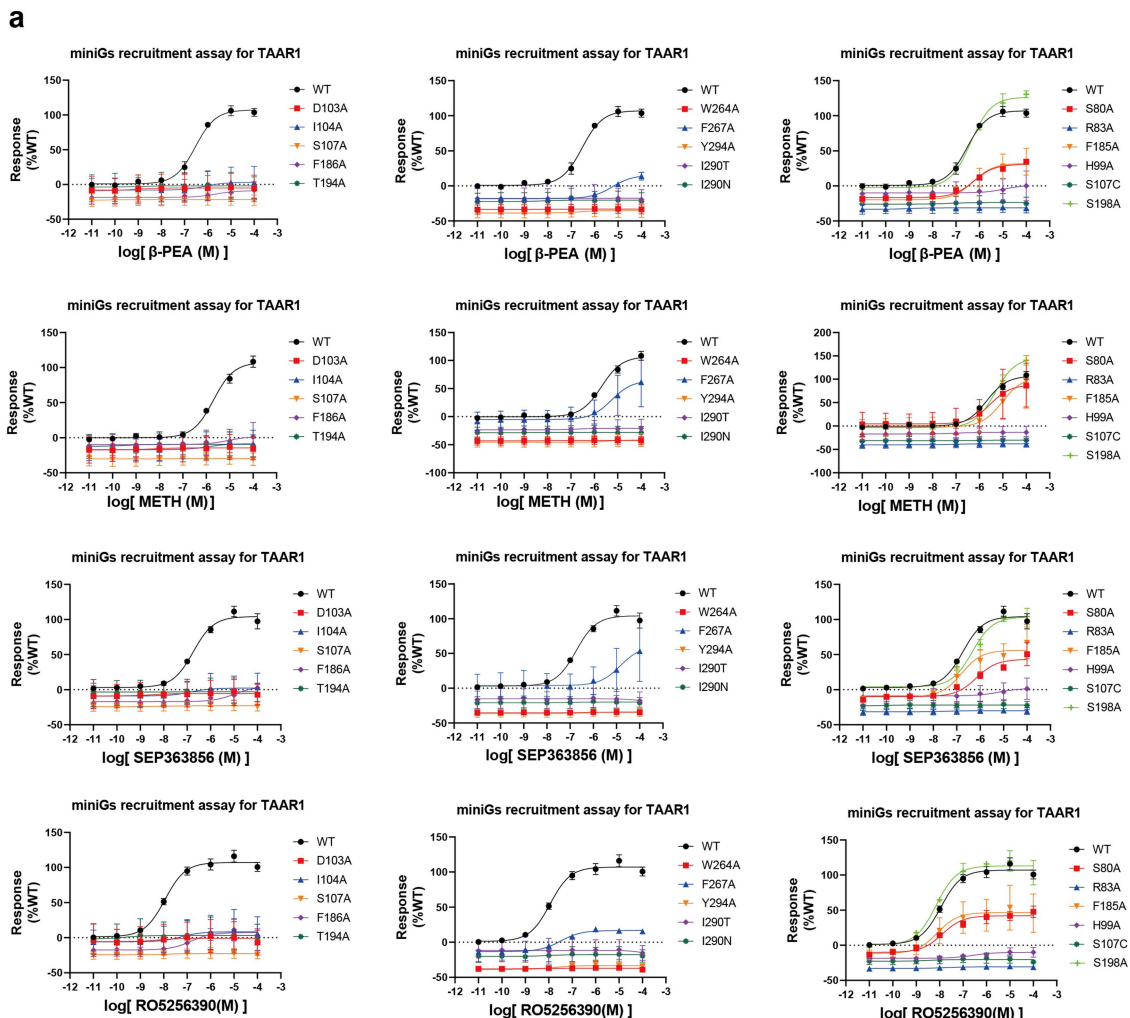
independent experiments ($n = 3$). (c) Structural comparison of ECL2s from TAAR1 and other aminergic receptors, ECL2 that forms a short helix in the structures is highlighted with red dotted circle.



Extended Data Fig. 2 | See next page for caption.

Article

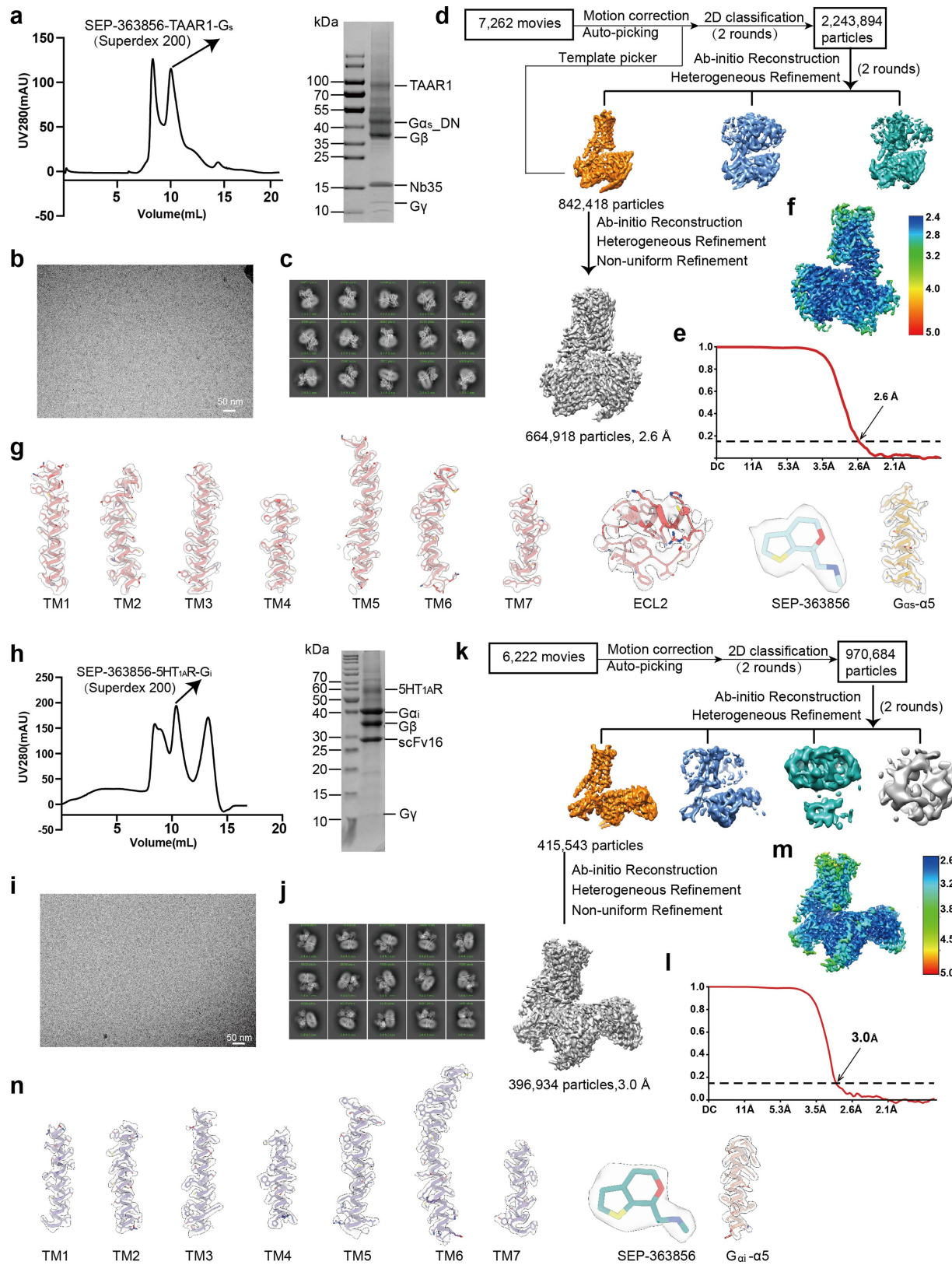
Extended Data Fig. 2 | Purification and structure determination of METH and β -PEA-bound TAAR1-G_s complexes. (a) Cartoon models of the two TAAR1 constructs used in this study. (b) Representative size exclusion chromatography (SEC) profiles and SDS-PAGE analysis of TAAR1-G_s complex activated by METH. Experiment was repeated at least three times with similar results. (c-d) Representative cryo-EM image from 6,686 movies (c) and 2D classification averages (d) of METH-TAAR1-G_s. (e) Cryo-EM data processing flowcharts of METH-TAAR1-G_s by cyroSPARC 3.2. (f) The Fourier shell correlation (FSC) curves of METH-TAAR1-G_s. The global resolution of the final processed density map estimated at the FSC = 0.143 is 2.8 Å. (g) The global density map of METH-TAAR1-G_s colored by local resolutions. (h) The density maps of helices TM1-TM7 of transmembrane domain, extracellular loop ECL2 of TAAR1, α 5 helix of G α _s, and METH in METH-TAAR1-G_s complex. (i) Representative size exclusion chromatography (SEC) profiles and SDS-PAGE analysis of TAAR1-G_s complex activated by β -PEA. Experiment was repeated at least three times with similar results. (j-k) Representative cryo-EM image from 4,371 movies (j) and 2D classification averages (k) of β -PEA-TAAR1-G_s. (l) Cryo-EM data processing flowcharts of β -PEA-TAAR1-G_s by cyroSPARC 3.2. (m) The Fourier shell correlation (FSC) curves of β -PEA-TAAR1-G_s. The global resolution of the final processed density map estimated at the FSC = 0.143 is 3.0 Å. (n) The global density map of β -PEA-TAAR1-G_s colored by local resolutions. (o) The density maps of helices TM1-TM7 of transmembrane domain, extracellular loop ECL2 of TAAR1, α 5 helix of G α _s, and β -PEA in β -PEA-TAAR1-G_s complex.



Extended Data Fig. 3 | Mutational effects of agonists and MD simulation analysis of TAAR1. (a) Concentration-response curves of wild-type/mutants of TAAR1 induced by the four agonists. Every response of mutant was normalized to corresponding wild-type as 100%. Data are mean \pm S.E.M. from 3 independent

experiments ($n = 3$). (b-c) RMSD plot of METH (b) or β -PEA (c) in TAAR1 pocket during simulations. (d) The free energy contribution of key residues in TAAR1 pocket for METH or β -PEA binding. Data are mean \pm S.E.M. from 6 independent experiments ($n = 6$).

Article

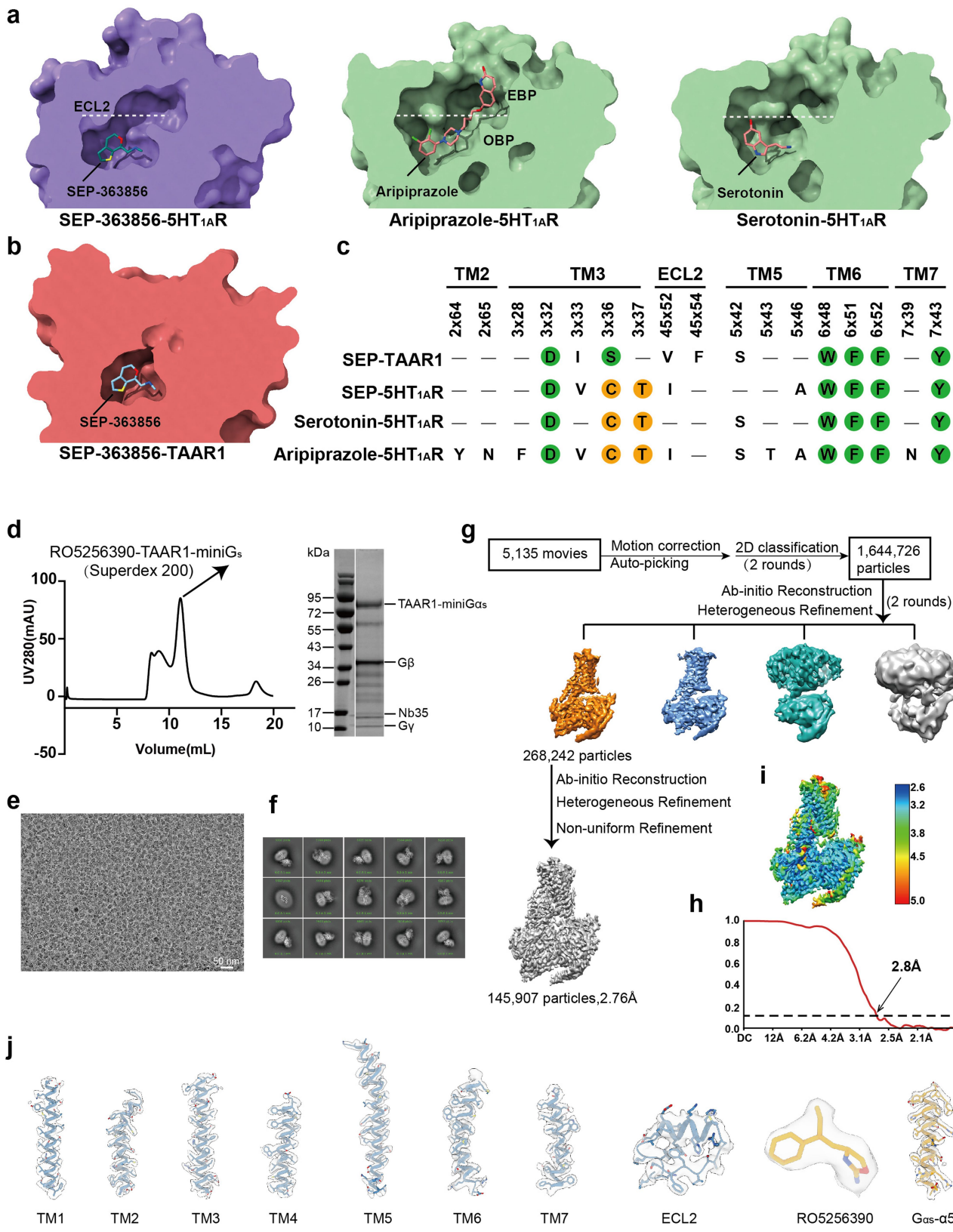


Extended Data Fig. 4 | See next page for caption.

Extended Data Fig. 4 | Purification and structure determination of SEP-363856 bound TAAR1-G_s and 5HT_{1A}R-G_i complexes. (a) Representative size exclusion chromatography (SEC) profiles and SDS-PAGE analysis of TAAR1-G_s complex activated by SEP-363856. Experiment was repeated at least three times with similar results. (b-c) Representative cryo-EM image from 7,262 movies (b) and 2D classification averages (c) of SEP-363856-TAAR1-G_s. (d) Cryo-EM data processing flowcharts of SEP-363856-TAAR1-G_s by cyroSPARC 3.2. (e) The Fourier shell correlation (FSC) curves of SEP-363856-TAAR1-G_s. The global resolution of the final processed density map estimated at the FSC = 0.143 is 2.6 Å. (f) The global density map of SEP-363856-TAAR1-G_s colored by local resolutions. (g) The density maps of helices TM1-TM7 of transmembrane domain, α5 helix of Gα_i, and SEP-363856 in 5HT_{1A}R-G_i complex.

in SEP-363856-TAAR1-G_s complex. (h) Representative size exclusion chromatography (SEC) profiles and SDS-PAGE analysis of 5HT_{1A}R-G_i complex activated by SEP-363856. Experiment was repeated at least three times with similar results. (i-j) Representative cryo-EM image from 6,222 movies (i) and 2D classification averages (j) of SEP-363856-5HT_{1A}R-G_i. (k) Cryo-EM data processing flowcharts of SEP-363856-5HT_{1A}R-G_i complex by cyroSPARC 3.2. (l) The Fourier shell correlation (FSC) curves of SEP-363856-5HT_{1A}R-G_i complex. The global resolution of the final processed density map estimated at the FSC = 0.143 is 3.0 Å. (m) The global density map of SEP-363856-5HT_{1A}R-G_i colored by local resolutions. (n) The density maps of helices TM1-TM7 of transmembrane domain, α5 helix of Gα_i, and SEP-363856 in 5HT_{1A}R-G_i complex.

Article

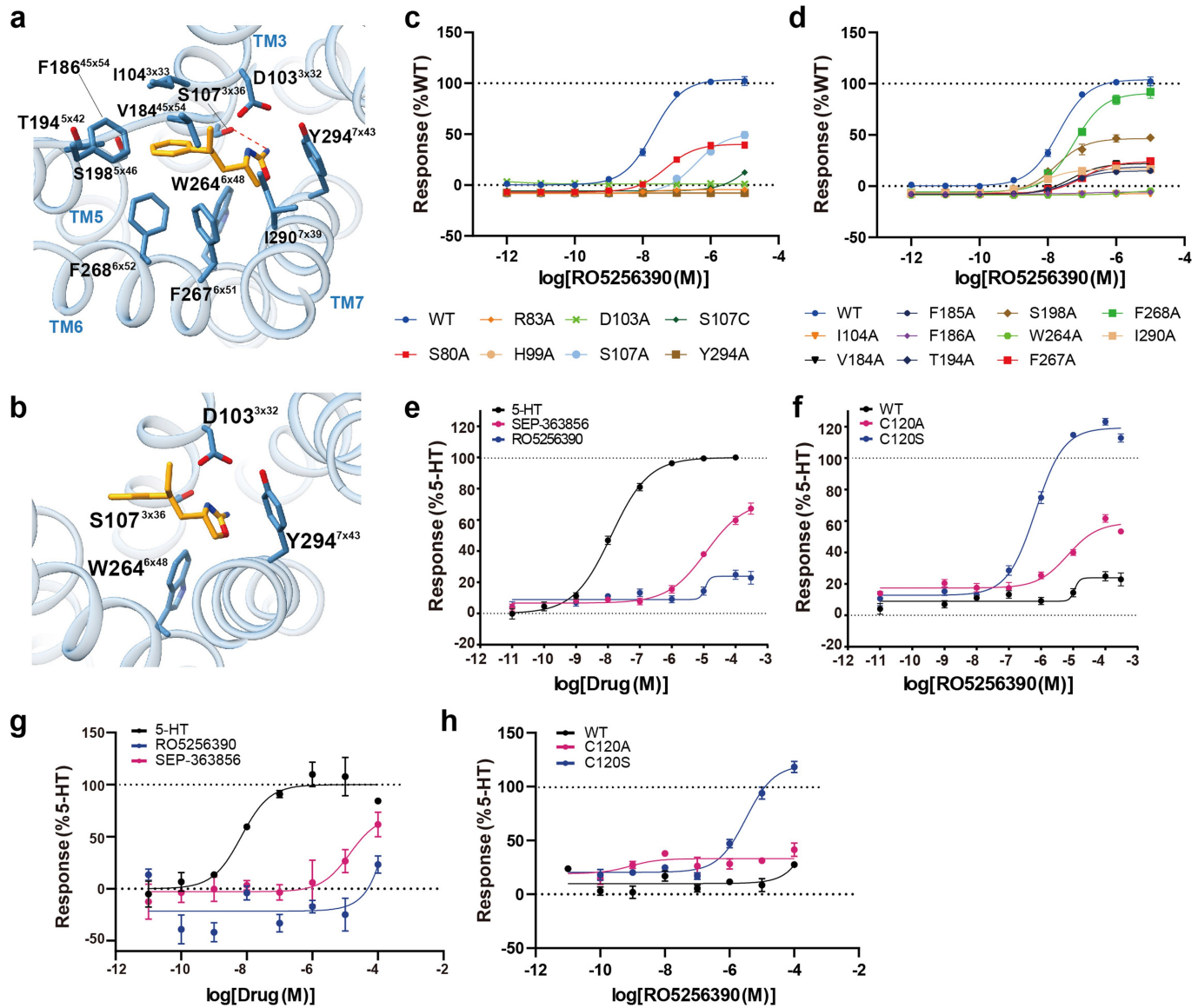


Extended Data Fig. 5 | See next page for caption.

Extended Data Fig. 5 | Comparison of the SEP-363856 bound pockets of TAAR1 and SHT_{1A}R, and purification, structure determination of RO5256390 bound TAAR1-G_s complex. (a) Binding pockets of SEP-363856, aripiprazole (PDB ID: 7e2z) and serotonin (PDB ID: 7e2y) in SHT_{1A}R. (b) Binding pocket of SEP-363856 in TAAR1. (c) Alignment of key residues constituting the ligand-binding pockets in SEP-383656 bound SHT_{1A}R or TAAR1 structures, and serotonin and aripiprazole bound SHT_{1A}R structures. The green background indicated 100% conserved residues and orange background indicated residues that are conserved in SHT_{1A}R but not in TAAR1. (d) Representative size exclusion chromatography (SEC) profiles and SDS-PAGE analysis of TAAR1-G_s complex

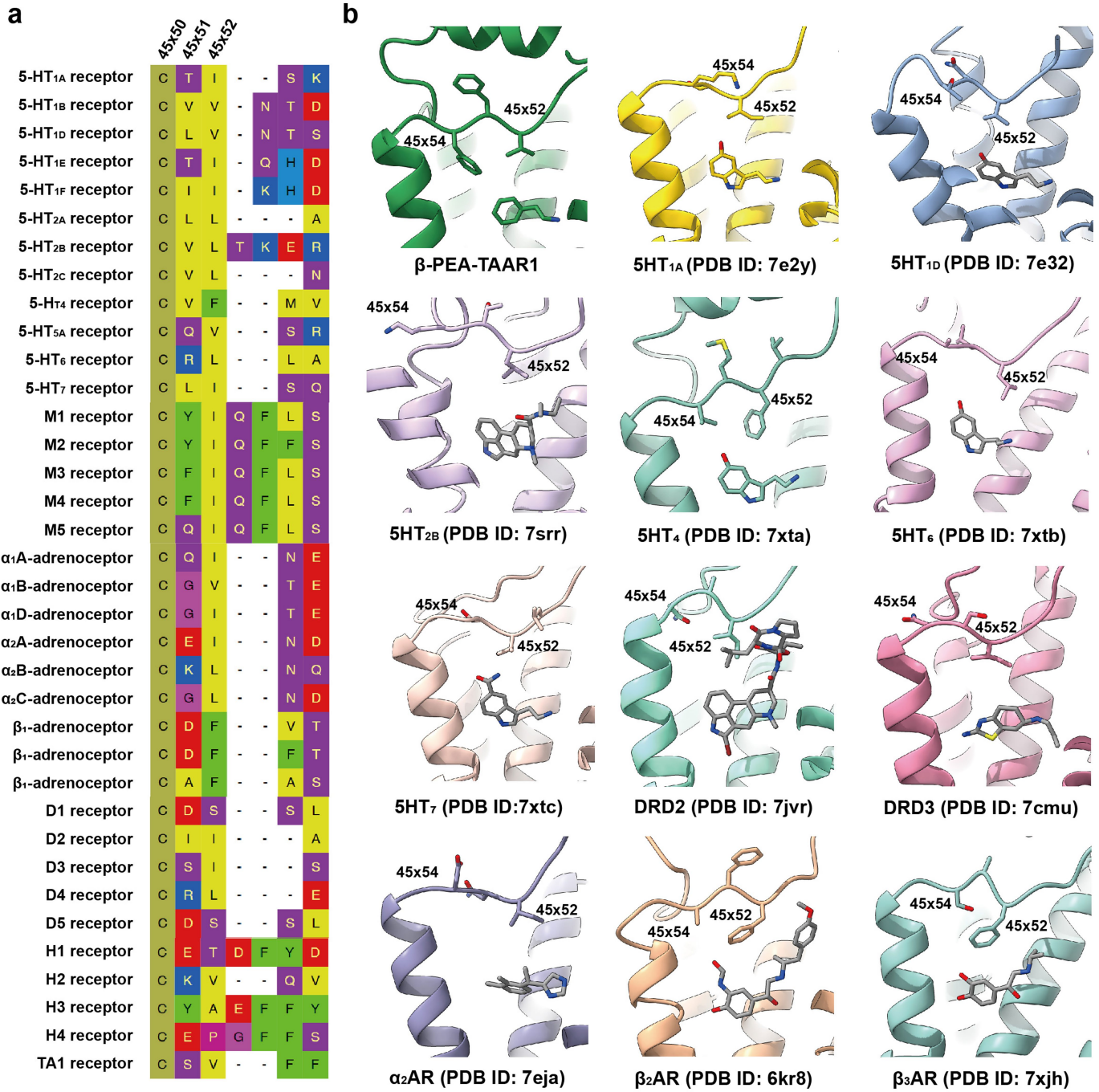
activated by RO5256390. Experiment was repeated at least three times with similar results. (e-f) Representative cryo-EM image from 5,135 movies (e) and 2D classification averages (f) of RO5256390-TAAR1-G_s. (g) Cryo-EM data processing flowcharts of RO5256390-TAAR1-G_s complex by cryoSPARC 3.2. (h) The Fourier shell correlation (FSC) curves of RO5256390-TAAR1-G_s. The global resolution of the final processed density map estimated at the FSC = 0.143 is 2.8 Å. (i) The global density map of RO5256390-TAAR1-G_s colored by local resolutions. (j) The density maps of helices TM1-TM7 of transmembrane domain, extracellular loop ECL2 of TAAR1, α 5 helix of G α _s, and RO5256390 in RO5256390-TAAR1-G_s complex.

Article



Extended Data Fig. 6 | Molecular mechanism of the high potency and selectivity of RO5256390. (a) Interactions of RO5256390 and key residues in TAAR1 pocket. (b) RO5256390 inserted deep into the cavity formed by D103^{3x32}, S107^{3x36}, W264^{6x48}, Y294^{7x43}. (c-d) Concentration–response curves for mutations of key residues in TAAR1 induced by RO5256390 using Glo-sensor assay. Data are mean \pm S.E.M. from 3 independent experiments ($n = 3$). (e) and (g) Evaluation

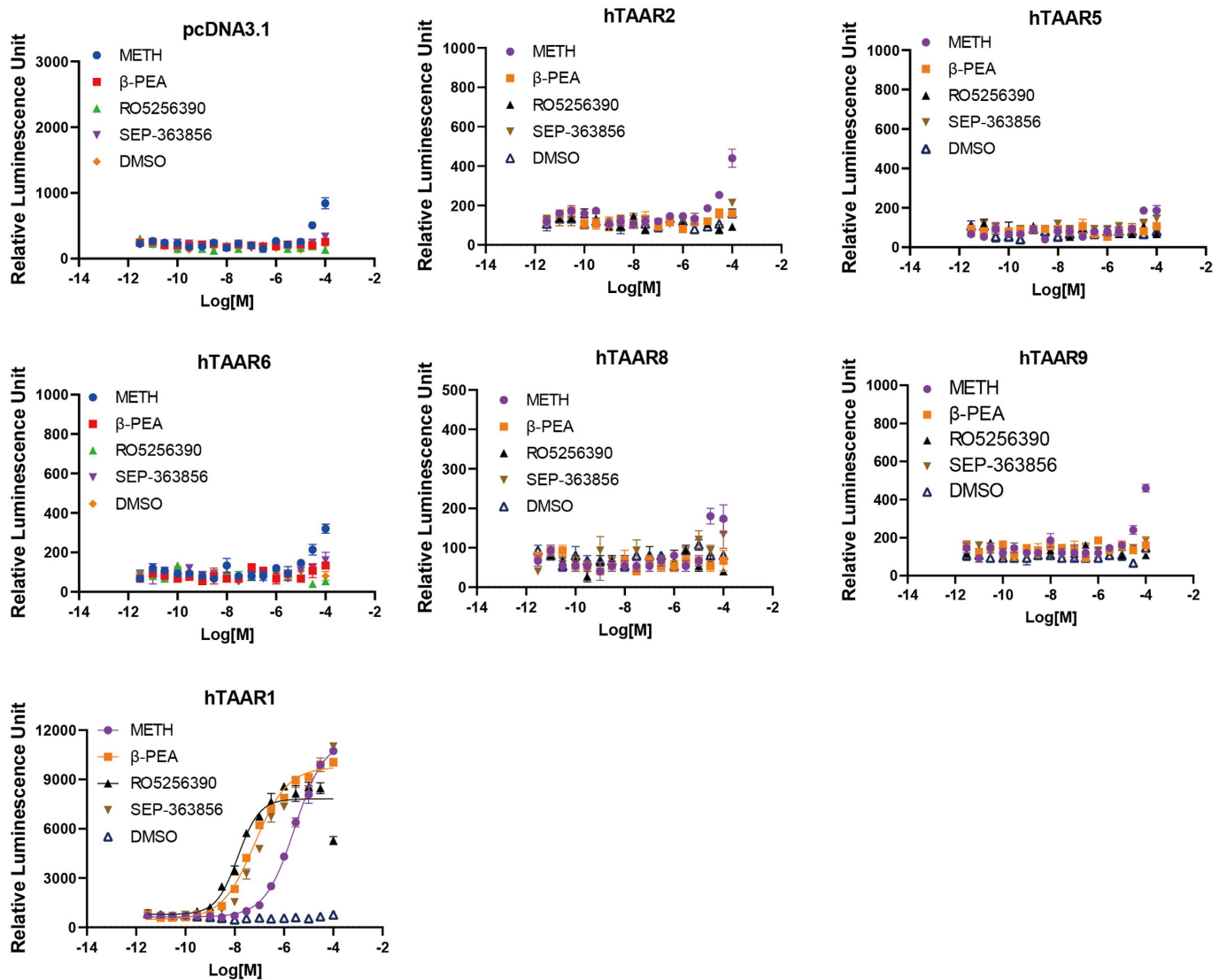
of RO5256390 and SEP-363856 activating 5HT_{1A}R using G_i protein dissociation assay (e) or Glo-sensor assay (g). 5HT was used as reference. Data are mean \pm S.E.M. from 3 independent experiments ($n = 3$). (f) and (h) Evaluation of RO5256390 activating 5HT_{1A}R with C120 substituted with alanine or serine, using G_i protein dissociation assay (f) or Glo-sensor assay (h). 5HT was used as reference. Data are mean \pm S.E.M. from 3 independent experiments ($n = 3$).



Extended Data Fig. 7 | Conservation of key residues for TAAR1 activating and role of ECL2 in aminergic receptors. (a) Sequence alignment of key residues in ECL2 from representative aminergic receptors. (b) Display of

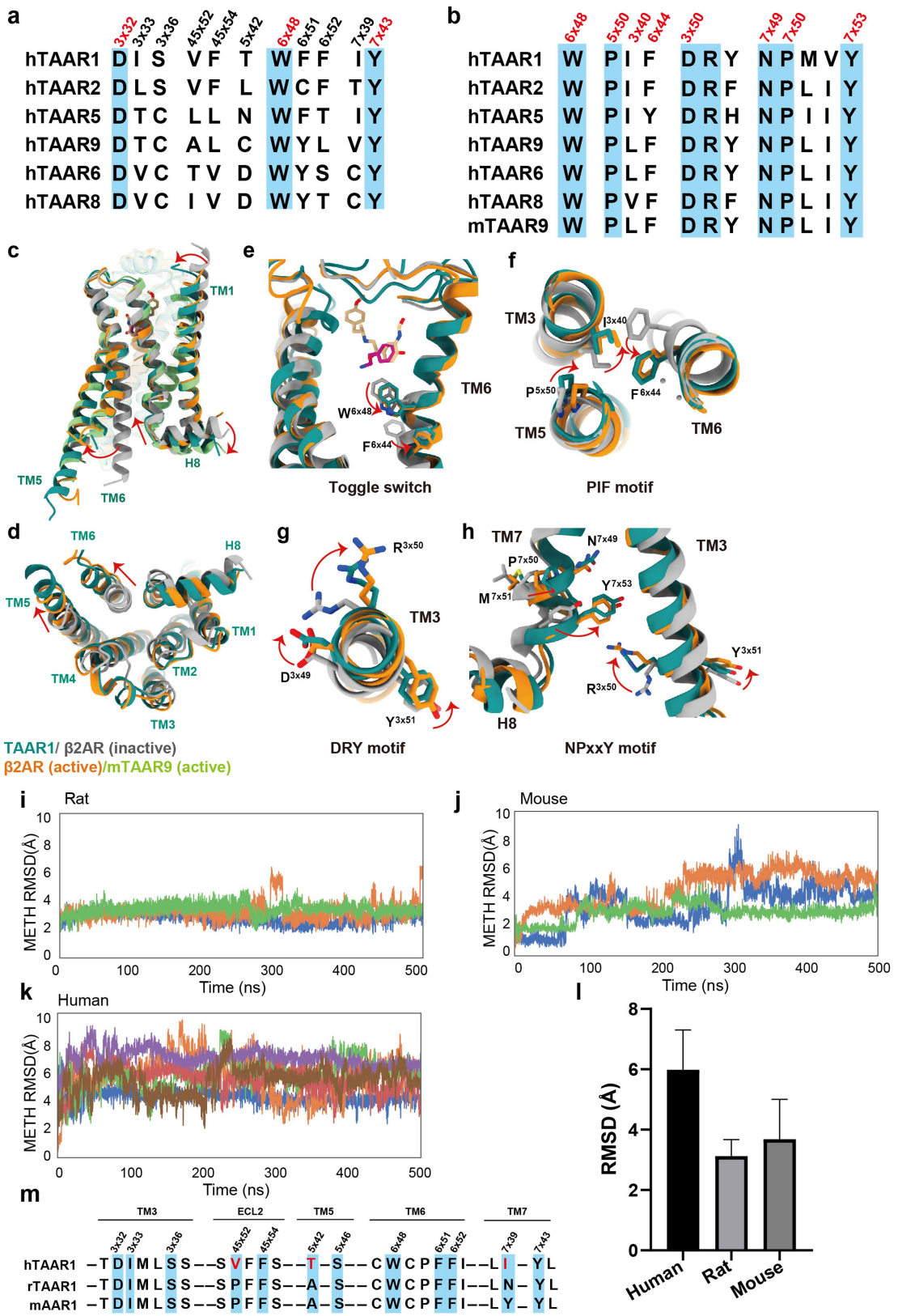
residues in ECL2s from TAAR1 and other aminergic receptors that may take part in ligand recognition and binding pocket formation.

Article



Extended Data Fig. 8 | Functional assessment of four agonists activating human TAAR family subtypes. Human TAAR family subtypes (hTAAR1/2/5/6/8/9) were cloned into pcDNA3.1 vector and the activity was measured by

Glo-Sensor assay. The negative control was pcDNA3.1 vector and DMSO solvent. The results showed that only TAAR1 can be activated by the four agonist. Data are mean \pm S.E.M. from 3 independent experiments ($n = 3$).



Extended Data Fig. 9 | See next page for caption.

Article

Extended Data Fig. 9 | Sequence alignment of human TAAR family, TAAR1 activation mechanism, and analysis of METH binding in human and rodent TAAR1. (a–b) Sequence alignment of residues important for TAAR1-ligand binding (a) or activating (b) from human TAAR family and mTAAR9. (c–d) Superposition of activated TAAR1 (dark cyan) with active mTAAR9 (light green; PDB ID: 8iw7), β_2 AR (orange; PDB ID: 6kr8) and inactive β_2 AR (gray; PDB ID: 5jqh). Notable conformational changes occur at extracellular end of TM1 and intracellular ends of TM6, TM7 and H8 upon receptor activation, side view (c) and bottom view (d). (e) The “toggle switch”, W264^{6,48}, of TAAR1 display

relative rotameric change when sensing agonist. (f–h) The key P-I-F^{6,44} (f), D-R^{3,50}-Y (g), and N-P^{7,50}-xx-Y^{7,53} (h) motifs displayed conformational rearrangement in activated TAAR1 structure. (i–k) RMSD plot of METH binding in rat, mouse, or human TAAR1 pocket during simulations. (l) Bar graph showing RMSD differences for METH binding in rat, mouse, or human TAAR1 pocket during simulations. Data are mean \pm S.E.M. of RMSD from 3 independent experiments ($n = 3$) for rat and mouse TAAR1 and 6 independent experiments ($n = 6$) for human TAAR1. (m) Sequence alignment for residues that are important for ligand binding to TAAR1 from rat, mouse or human.

Extended Data Table 1 | Cryo-EM data collection, refinement and validation statistics

	TAAR1-Gαs				5HT1AR-Gαi
	METH	β-PEA	RO5256390	SEP-363856	SEP-363856
Magnification	96,000	105,000	105,000	105,000	105,000
Voltage (kV)	300	300	300	300	300
Electron exposure (e ⁻ /Å ²)	50	60	60	50	50
Defocus range (μm)	-1.0 to -2.0	-1.0 to -2.0	-1.0 to -2.0	-1.0 to -2.0	-1.0 to -2.0
Pixel size (Å)	0.73	0.832	0.832	0.824	0.824
Symmetry imposed	C1	C1	C1	C1	C1
Filtered particle images (no.)	928,277	556,800	1,644,726	824,418	970,684
Final particle images (no.)	483,727	87,235	145,907	664,918	396,934
Map resolution (Å)	2.8	3.0	2.8	2.6	3.0
FSC threshold	0.143	0.143	0.143	0.143	0.143
Map resolution range (Å)	2.6 - 5.0	2.6 - 5.0	2.6 - 5.0	2.5 - 5.0	2.6 - 5.0
Refinement					
Initial model used (PDB code)	AlphaFold TAAR1	AlphaFold TAAR1	AlphaFold TAAR1	AlphaFold TAAR1	7e2y
Map sharpening <i>B</i> factor (Å ²)	-109.2	-80	-60	-122.8	-137.3
Model composition					
Non-hydrogen atoms	8,256	8,230	8,263	8,307	8,764
Protein residues	1,046	1,043	1,045	1,039	1,100
Ligands	1	1	1	1	1
<i>B</i> factors (Å ²)					
Protein	98.16	65.82	70.36	29.47	72.94
Ligand	20.00	53.93	66.12	46.55	84.13
R.m.s. deviations					
Bond lengths (Å)	0.005	0.006	0.005	0.005	0.004
Bond angles (°)	0.984	0.825	0.709	0.968	0.917
Validation					
MolProbity score	1.27	1.47	1.38	1.33	1.21
Clashscore	4.16	4.84	4.95	3.99	3.36
Poor rotamers (%)	0.00	0.00	0.00	0.00	0.00
Ramachandran plot					
Favored (%)	97.87	96.61	97.39	97.26	97.59
Allowed (%)	2.13	3.39	2.61	2.74	2.41
Disallowed (%)	0.00	0.00	0.00	0.00	0.00

Reporting Summary

Nature Portfolio wishes to improve the reproducibility of the work that we publish. This form provides structure for consistency and transparency in reporting. For further information on Nature Portfolio policies, see our [Editorial Policies](#) and the [Editorial Policy Checklist](#).

Statistics

For all statistical analyses, confirm that the following items are present in the figure legend, table legend, main text, or Methods section.

n/a Confirmed

- The exact sample size (n) for each experimental group/condition, given as a discrete number and unit of measurement
- A statement on whether measurements were taken from distinct samples or whether the same sample was measured repeatedly
- The statistical test(s) used AND whether they are one- or two-sided
Only common tests should be described solely by name; describe more complex techniques in the Methods section.
- A description of all covariates tested
- A description of any assumptions or corrections, such as tests of normality and adjustment for multiple comparisons
- A full description of the statistical parameters including central tendency (e.g. means) or other basic estimates (e.g. regression coefficient) AND variation (e.g. standard deviation) or associated estimates of uncertainty (e.g. confidence intervals)
- For null hypothesis testing, the test statistic (e.g. F , t , r) with confidence intervals, effect sizes, degrees of freedom and P value noted
Give P values as exact values whenever suitable.
- For Bayesian analysis, information on the choice of priors and Markov chain Monte Carlo settings
- For hierarchical and complex designs, identification of the appropriate level for tests and full reporting of outcomes
- Estimates of effect sizes (e.g. Cohen's d , Pearson's r), indicating how they were calculated

Our web collection on [statistics for biologists](#) contains articles on many of the points above.

Software and code

Policy information about [availability of computer code](#)

Data collection Cryo-EM data collection on the Titan Krios using EPU 3.4.0.5704REL and Serial EM.

Data analysis cryoSPARC v3.2, MotionCor2, Phenix 1.20, Coot 0.9.6, Pymol 2.0, ISOLDE-1.2, UCSF ChimeraX-1.2, UCSF Chimera-1.14, GraphPad Prism 8.0, GraphPad Prism 9.0, MODELLER10.2, Maestro12.8, PROPKA3.0, Amber20, AmberTools20

For manuscripts utilizing custom algorithms or software that are central to the research but not yet described in published literature, software must be made available to editors and reviewers. We strongly encourage code deposition in a community repository (e.g. GitHub). See the Nature Portfolio [guidelines for submitting code & software](#) for further information.

Data

Policy information about [availability of data](#)

All manuscripts must include a [data availability statement](#). This statement should provide the following information, where applicable:

- Accession codes, unique identifiers, or web links for publicly available datasets
- A description of any restrictions on data availability
- For clinical datasets or third party data, please ensure that the statement adheres to our [policy](#)

All data produced or analyzed in this study are included in the main text or the supplementary materials. A reporting summary for this article is available as Supplementary information file. Density maps and structure coordinates have been deposited in the Electron Microscopy Data Bank (EMDB) and the Protein Data

Bank (PDB) with accession codes EMD-37347 and 8W87 for METH-TAAR1-Gs complex; EMD-37348 and 8W88 for SEP363856-bound TAAR1-Gs complex; and EMD-37349 and 8W89 for PEA-bound TAAR1-Gs complex; EMD-37350 and 8W8A for RO5256390-TAAR1-Gs complex; and EMD-37351 and 8W8B for SEP-363856 bounded serotonin 1A (5-HT1A) receptor-Gi protein complex.

Research involving human participants, their data, or biological material

Policy information about studies with [human participants or human data](#). See also policy information about [sex, gender \(identity/presentation\), and sexual orientation](#) and [race, ethnicity and racism](#).

Reporting on sex and gender

N/A

Reporting on race, ethnicity, or other socially relevant groupings

N/A

Population characteristics

N/A

Recruitment

N/A

Ethics oversight

N/A

Note that full information on the approval of the study protocol must also be provided in the manuscript.

Field-specific reporting

Please select the one below that is the best fit for your research. If you are not sure, read the appropriate sections before making your selection.

Life sciences Behavioural & social sciences Ecological, evolutionary & environmental sciences

For a reference copy of the document with all sections, see nature.com/documents/nr-reporting-summary-flat.pdf

Life sciences study design

All studies must disclose on these points even when the disclosure is negative.

Sample size

For structural determination, 6,686 movies of METH-TAAR1-Gs complex, 4,371 movies of β -PEA-TAAR1-Gs complex, 7,262 movies of SEP-363856-TAAR1-Gs complex, 6,222 movies of SEP-363856-5HT1A-Gi complex and 5,135 movies of RO5256390-TAAR1-Gs complex were collected. For Glo-Sensor cAMP assay, Gs recruitment, Radioligand binding and G α i β dissociation, at least three biologically independent experiments/n=3) were performed as depicted in related Figure legends. Data were analyzed by fitting various ligand concentrations and readouts using appropriate equations in GraphPad Prism 8.0 and GraphPad Prism 9.0.

Data exclusions

No data were excluded

Replication

Each experiment was reproduced at least three times on separate occasions. Experimental findings were reliably reproduced.

Randomization

No randomization was attempted or needed. Randomization was not necessary as the independent variables to be tested were sufficient for the functional interpretation within this study. i.e. WT vs mutant vs control conditions or dose-response determination.

Blinding

Blinding is not necessary or valid for the purposes of structural determination. For cyro-EM study, purified ligand bound TAAR1 or 5HT1A G protein complex were applied onto a glow-discharged holey carbon grid and subsequently vitrified using a Vitrobot Mark V. Cryo-EM imaging was performed on a Titan Krios equipped with a Gatan K3 or Falcon 4 direct electron detector. The microscope was operated at 300 kV accelerating voltage. Finally, 6,686 movies of METH-TAAR1-Gs complex, 4,371 movies of β -PEA-TAAR1-Gs complex, 7,262 movies of SEP-363856-TAAR1-Gs complex, 6,222 movies of SEP-363856-5HT1A-Gi complex and 5,135 movies of RO5256390-TAAR1-Gs complex were collected with defocus range from -1.0 to 2.0 μ m. For functional analysis, blinding was not necessary due to the quantitative nature of the experiment. All experimental data acquired or analyzed in this study are included in this published article, and subjected to statistical analysis whenever necessary.

Reporting for specific materials, systems and methods

We require information from authors about some types of materials, experimental systems and methods used in many studies. Here, indicate whether each material, system or method listed is relevant to your study. If you are not sure if a list item applies to your research, read the appropriate section before selecting a response.

Materials & experimental systems

n/a	Involved in the study
<input type="checkbox"/>	<input checked="" type="checkbox"/> Antibodies
<input type="checkbox"/>	<input checked="" type="checkbox"/> Eukaryotic cell lines
<input checked="" type="checkbox"/>	<input type="checkbox"/> Palaeontology and archaeology
<input checked="" type="checkbox"/>	<input type="checkbox"/> Animals and other organisms
<input checked="" type="checkbox"/>	<input type="checkbox"/> Clinical data
<input checked="" type="checkbox"/>	<input type="checkbox"/> Dual use research of concern
<input checked="" type="checkbox"/>	<input type="checkbox"/> Plants

Methods

n/a	Involved in the study
<input checked="" type="checkbox"/>	<input type="checkbox"/> ChIP-seq
<input type="checkbox"/>	<input checked="" type="checkbox"/> Flow cytometry
<input checked="" type="checkbox"/>	<input type="checkbox"/> MRI-based neuroimaging

Antibodies

Antibodies used

Nb35 and scFv16 were used to stabilize the complex. The Brian K. Kobilka laboratory reported the sequence of Nb35, generated from a camelid antibody fragment (DOI:10.1038/nature10361), and scFv16, derived from the mouse monoclonal antibody mAb16 (DOI:10.1038/s41467-018-06002-w). Nb35 packs at the interface of the G β and G α subunits to stabilize the complex. It was cloned into the pFastBac vector (Thermo Fisher) and co-expressed with receptor-Gs protein complexes in Spodopterafrugiperda SF9 insect cells (Invitrogen) using the baculovirus method (Expression Systems). ScFv16 stabilizes GPCR/G-protein complexes by recognizing an interface between G α and G β subunits in the heterotrimer. The gene was cloned into the pFastBac vector (Thermo Fisher) and co-expressed with receptor-Gi protein complexes in SF9 insect cells (Invitrogen) using the baculovirus method (Expression Systems). Anti-FLAG M2 antibody (Sigma, Cat. F3165) and anti-mouse Alexa Fluor 488 conjugated secondary antibody (Invitrogen, Cat. A11029) were used for surface expression measurement.

Validation

Nb35 can bind and stabilize the Gs heterotrimer. The characterization of Nb35 was reported by Rasmussen et al. DOI:10.1038/nature10361. ScFv16 recognizes the interface between G α and G β subunits in the heterotrimer reported in DOI:10.1038/s41467-018-06002-w. Anti-Flag M2 antibody is used for the detection of Flag fusion proteins. This monoclonal antibody is produced in mouse and recognizes the FLAG sequence at the N-terminus, Met N-terminus, and C-terminus. The antibody is also able to recognize FLAG at an internal site. Invitrogen™ Alexa Fluor 488 dye is a bright, green-fluorescent dye with excitation ideally suited to the 488 nm laser line. For stable signal generation in imaging and flow cytometry, Alexa Fluor 488 dye is pH-insensitive over a wide molar range. All commercial antibodies are validated by the supplier using sensitivity tests, electrophoresis and Western blots.

Eukaryotic cell lines

Policy information about [cell lines](#) and [Sex and Gender in Research](#)

Cell line source(s)

SF9 cells were obtained from Expression Systems (Cat 94-001S), High five cells from invitogen (B85502) and HEK293 cells from the American Type Culture Collection (ATCC, CRL-1573).

Authentication

None of the cell lines have been authenticated.

Mycoplasma contamination

All cell lines were tested negative for mycoplasma contamination.

Commonly misidentified lines (See [ICLAC](#) register)

No commonly misidentified lines were used.

Flow Cytometry

Plots

Confirm that:

- The axis labels state the marker and fluorochrome used (e.g. CD4-FITC).
- The axis scales are clearly visible. Include numbers along axes only for bottom left plot of group (a 'group' is an analysis of identical markers).
- All plots are contour plots with outliers or pseudocolor plots.
- A numerical value for number of cells or percentage (with statistics) is provided.

Methodology

Sample preparation

Sample preparation is listed in Methods.

Instrument

Guava easyCyte 8HT (Merck Millipore); Accuri C6 flow cytometer (BD biosciences)

Software

Guava software 3.1; Accuri C6 flow cytometer software

Cell population abundance

Approximately 10,000 cellular events were collected and the total fluorescence intensity of positive expression

Gating strategy

Gating was determined by the fluorescent intensity of FITC to differentiate positive cells and all other cells.

Tick this box to confirm that a figure exemplifying the gating strategy is provided in the Supplementary Information.